



저작자표시-비영리-변경금지 2.0 대한민국

이용자는 아래의 조건을 따르는 경우에 한하여 자유롭게

- 이 저작물을 복제, 배포, 전송, 전시, 공연 및 방송할 수 있습니다.

다음과 같은 조건을 따라야 합니다:



저작자표시. 귀하는 원저작자를 표시하여야 합니다.



비영리. 귀하는 이 저작물을 영리 목적으로 이용할 수 없습니다.



변경금지. 귀하는 이 저작물을 개작, 변형 또는 가공할 수 없습니다.

- 귀하는, 이 저작물의 재이용이나 배포의 경우, 이 저작물에 적용된 이용허락조건을 명확하게 나타내어야 합니다.
- 저작권자로부터 별도의 허가를 받으면 이러한 조건들은 적용되지 않습니다.

저작권법에 따른 이용자의 권리는 위의 내용에 의하여 영향을 받지 않습니다.

이것은 [이용허락규약\(Legal Code\)](#)을 이해하기 쉽게 요약한 것입니다.

[Disclaimer](#)

의학박사 학위논문

**Enhanced Hepatobiliary Excretion of  
Micelle encapsulated  
Upconverting Nanoparticles  
using *in vivo* PET and Optical Imaging**

마이셀 피막화된 Upconverting 나노입자의  
체내 PET과 광학영상을 이용한  
향상된 간담체 배설

2015 년 8월

서울대학교 융합과학기술대학원  
분자의학 및 바이오제약학과  
서 효 정

**Enhanced Hepatobiliary Excretion of  
Micelle encapsulated Upconverting Nanoparticles  
using *in vivo* PET and Optical Imaging**

지도교수 이 동 수

이 논문을 의학박사 학위논문으로 제출함

2015년 4 월

서울대학교 융합과학기술대학원

분자의학 및 바이오제약학과

서 효 정

서효정의 의학박사 학위논문을 인준함

2015년 6 월

위 원 장 \_\_\_\_\_ (인)

부위원장 \_\_\_\_\_ (인)

위 원 \_\_\_\_\_ (인)

위 원 \_\_\_\_\_ (인)

위 원 \_\_\_\_\_ (인)

# Contents

<b>CONTENTS.....</b>	<b>3</b>
<b>ABSTRACT.....</b>	<b>6</b>
<b>LIST OF ABBREVIATIONS.....</b>	<b>13</b>
<b>INTRODUCTION.....</b>	<b>14</b>
<b>PURPOSE.....</b>	<b>19</b>
<b>MATERIALS AND METHODS.....</b>	<b>20</b>
Chemicals.....	20
Synthesis of hexagonal phase NaYF <sub>4</sub> :Yb <sup>3+</sup> /Er <sup>3+</sup> nanoparticles (UCNPs).....	20
Synthesis of ligands conjugated with stearyl chains (NOTA-C <sub>18</sub> ).....	21
Encapsulation of UCNPs with amphiphiles.....	21
Stability Test.....	22
<sup>64</sup> Cu Radiolabeling.....	22
<i>In vivo</i> microPET imaging of micelle encapsulated <sup>64</sup> Cu-NOTA-UCNPs,	

$^{64}\text{Cu}$ -NOTA- $\text{C}_{18}$ and free $^{64}\text{Cu}$ injected mice.....	23
Biodistribution study using micelle encapsulated $^{64}\text{Cu}$ -NOTA-UCNPs and <i>ex vivo</i> method.....	28
Preparation of intraluminal feces, feces and urine smear section for upconversion luminescence imaging .....	28
Upconversion luminescence spectra of UCNPs.....	29
Acquisition of upconversion luminescence imaging.....	30
Acquisition of TEM .....	30
Statistical analysis.....	31
<b>RESULTS.....</b>	<b>32</b>
<b>Part I. Characteristics of micelle encapsulated <math>^{64}\text{Cu}</math>-NOTA-UCNPs.....</b>	<b>32</b>
Synthesis of micelle encapsulated $^{64}\text{Cu}$ -NOTA-UCNPs.....	32
Purity, size and zeta potential.....	32
Stability test.....	33
<b>Part II. Multimodal imaging and quantification of hepatobiliary excretion of micelle encapsulated <math>^{64}\text{Cu}</math>-NOTA-UCNPs.....</b>	<b>38</b>
<i>In vivo</i> biodistribution study of whole body microPET imaging....	38
Quantification of <i>in vivo</i> whole body microPET imaging.....	40

<i>Ex vivo</i> biodistribution study and quantification.....	42
<i>In vivo, in situ</i> and <i>ex vivo</i> upconversion luminescence imaging...	45
<b>Part III. Evidence of hepatobiliary excretion of micelle encapsulated <sup>64</sup>Cu-NOTA-UCNPs.....</b>	<b>49</b>
Comparison of <i>in vivo</i> PET images using free <sup>64</sup> Cu, <sup>64</sup> Cu-NOTA-C <sub>18</sub> and <sup>64</sup> Cu-NOTA-UCNPs.....	49
PET and upconversion luminescence images and <i>ex vivo</i> method of feces and urine.....	54
TEM study of hepatobiliary excretion.....	58
<b>DISCUSSION.....</b>	<b>62</b>
<b>CONCLUSION.....</b>	<b>81</b>
국문초록.....	98

# **Abstract**

## **Enhanced Hepatobiliary Excretion of Micelle encapsulated Upconverting Nanoparticles using *in vivo* PET and Optical Imaging**

**Hyo Jung Seo**

*Department of Molecular Medicine and Biopharmaceutical Science,  
The Graduate School of Convergence Science and Technology,  
Seoul National University*

### **Purpose:**

Nanoparticle (NP) accumulation and toxicity in variable organs have been an obstacle for biomedical application. Therefore, the characteristics of good excretion and biocompatibility of NPs are very important. One of the candidate biocompatible NPs, upconverting nanoparticle (UCNP) has emerged for

biomedical application recently. Herein, I demonstrated that micelle encapsulated  $^{64}\text{Cu}$ -labeled upconverting nanoparticles (micelle encapsulated  $^{64}\text{Cu}$ -NOTA-UCNPs) showed substantial hepatobiliary excretion within 24 hours by *in vivo* positron emission tomography (PET) and also upconversion luminescence imaging (ULI). A long half-life (762 min) radiotracer  $^{64}\text{Cu}$  is a competent material to evaluate biodistribution and quantification for 72 hours. And I quantified the excretion of micelle encapsulated  $^{64}\text{Cu}$ -NOTA-UCNPs by PET and *ex vivo* method and revealed the excretory pathway by PET, ULI and transmission electron microscopy (TEM).

### **Methods:**

$\text{NaYF}_4:\text{Yb}^{3+}, \text{Er}^{3+}$  NPs (UCNPs) were encapsulated and labeled with NOTA- $\text{C}_{18}$  and  $^{64}\text{Cu}$ . After micelle encapsulated  $^{64}\text{Cu}$ -NOTA-UCNPs was intravenously injected in 6-week-old male BALB/c nude mice (weight =  $24.1 \pm 0.5$  g, dose =  $40 \pm 0.6 \mu\text{Ci}/50 \mu\text{L}$ , n = 7), whole body microPET was performed to obtain serial time point images (0.25, 1, 2, 4, 8, and 24 hours, n = 3 / 0.25, 1, 2, 4, 8, 24, 48 and 72 hours, n = 4) for *in vivo* biodistribution. To compare study of free  $^{64}\text{Cu}$  (n = 3),  $^{64}\text{Cu}$ -NOTA- $\text{C}_{18}$  (n = 3) and  $^{64}\text{Cu}$ -NOTA-UCNPs (n = 7), microPET was performed as serial time points (0.25, 1, 2, 4, 8, and 24 hours). For *ex vivo* biodistribution, micelle encapsulated  $^{64}\text{Cu}$ -NOTA-UCNPs were injected into a male BALB/c mouse via the tail vein (weight =  $20.1 \pm 0.5$  g, dose =  $1 \mu\text{Ci}/100 \mu\text{L}$ ). The injected mice were sacrificed in serial time points (1, 4, 8, 24, and 72 hours, 3 mice for collection of feces and urine, n = 3, respectively, total n = 18) of post-

injection. For ULI biodistribution study, UCNPs were injected intravenously in BALB/c nude mice (weight =  $24.1 \pm 0.5$  g, dose = 0.158 mg/300  $\mu$ L, total n = 7). *In vivo*, *in situ* and *ex vivo* ULIs were obtained as serial time points (1, 2, 4, 8, and 24 hours). Collected feces and urine were evaluated by microPET and ULI. Extracted liver was evaluated by TEM to reveal the hepatobiliary excretion as two time points (1 hour, n = 3, and 24 hours, n = 4).

### **Results:**

Using micelle encapsulation method, the final yield of micelle encapsulated  $^{64}\text{Cu}$ -NOTA-UCNPs was 40%. The radiochemical purity of micelle encapsulated  $^{64}\text{Cu}$ -NOTA-UCNPs was 99%. *In vivo* whole body microPET image revealed the remarkable hepatobiliary excretion according to the delayed time points. Hepatic uptake persisted until 8 hour delay image, but it was markedly decreased at 24 hour delay image and further decreased until 72 hours. Linearly increased uptake along the bowel was shown after 1 hour and the uptake was further extended along the intestine at 2, 4 and 8 hour delay images. Also, micelle encapsulated  $^{64}\text{Cu}$ -NOTA-UCNPs showed faster hepatic excretion than free  $^{64}\text{Cu}$  and the biodistribution of micelle encapsulated  $^{64}\text{Cu}$ -NOTA-UCNPs was different from that of  $^{64}\text{Cu}$ -NOTA- $\text{C}_{18}$ .

Similarly, in our *ex vivo* biodistribution study, over 80% clearance from initial liver uptake within 72 hours and over 40% of total injected dose excretion by feces within 24 hours after injection of NPs have been revealed. The concentration of liver was increased till 8 hours and markedly decreased at 24 hours. Gradual

increase of the concentration of intestine had been manifested till 8 hours and the concentration of intestine was decreased at 24 hours. Collected feces in *ex vivo* biodistribution consisted of 40.9%.

Likewise, *in vivo*, *in situ* and *ex vivo* ULI revealed good hepatobiliary excretion. However, we could not obtain the sufficient signal for *in vivo* ULI which was 13 times higher amount (158  $\mu\text{g}/\text{mouse}$ ) than that for the dose of PET imaging (12  $\mu\text{g}/\text{mouse}$ ). In 1 hour post-injection *ex vivo* image, liver, spleen and lung showed positive signals which were consistent with PET image. The intestinal uptake was not well-visualized in *in vivo* image, but after extraction and exposure of intestinal lumen, UCNP signal was clearly detected.

Additionally, the evidences of hepatobiliary excretion of micelle encapsulated  $^{64}\text{Cu}$ -NOTA-UCNPs were obtained by ULI, PET and TEM. ULI revealed UCNP signal in all collected feces and urine. PET showed excretory  $^{64}\text{Cu}$ -NOTA-UCNPs in all collected feces. In TEM images, UCNPs were observed inside of sinusoid, space of Disse, hepatocyte, Kupffer cells and bile canaliculi at 1 hour after injection. However, NP was not found inside of hepatocyte, but remained in Kupffer cells at 24 hours after injection.

### **Conclusions:**

In conclusion, I demonstrated the feasibility of bimodal *in vivo* imaging characteristics of micelle encapsulated  $^{64}\text{Cu}$ -NOTA-UCNP and showed the substantial hepatobiliary excretion through *in vivo* microPET, ULI, and *ex vivo*

biodistribution study. This bimodal imaging characteristic is ideal for the evaluation of excretion pattern of NP, because PET imaging is suitable for accurate quantification of biodistribution and ULI can be used for the confirmation of UCNP. Moreover, by well characterization of imaging property and excretion pattern of micelle encapsulated  $^{64}\text{Cu}$ -NOTA-UCNPs, NPs could be used for bimodal ULI and PET imaging agent for a variety of purposes by adding further functional moiety.

**Key words:** Upconverting nanoparticle, Positron emission tomography (PET), Optical imaging, Hepatobiliary excretion, Transmission electron microscopy (TEM)

**Student number: 2012-30798**

## List of Figures

<b>Figure 1.</b> <i>Experimental design</i> .....	27
<b>Figure 2.</b> <i>Schematic illustration for synthesis of micelle encapsulated <sup>64</sup>Cu-NOTA-UCNP</i> .....	34
<b>Figure 3.</b> <i>TEM images of UCNPs and micelle encapsulated <sup>64</sup>Cu-NOTA-UCNP</i> .....	35
<b>Figure 4.</b> <i>The hydrodynamic size and zeta potential of UCNPs, and micelle encapsulated <sup>64</sup>Cu-NOTA-UCNPs</i> .....	36
<b>Figure 5.</b> <i>Stability test of micelle encapsulated <sup>64</sup>Cu-NOTA-UCNPs</i> .....	37
<b>Figure 6.</b> <i>In vivo whole body microPET imaging</i> .....	39
<b>Figure 7.</b> <i>Quantification of in vivo whole body microPET imaging</i> .....	41
<b>Figure 8.</b> <i>Quantification of ex vivo biodistribution study</i> .....	43
<b>Figure 9.</b> <i>Quantification of ex vivo biodistribution study according to organs</i> .....	44
<b>Figure 10.</b> <i>In vivo and in situ upconversion luminescence imaging</i> .....	46
<b>Figure 11.</b> <i>Ex vivo upconversion luminescence imaging</i> .....	48
<b>Figure 12.</b> <i>Comparison of in vivo PET images using free <sup>64</sup>Cu , <sup>64</sup>Cu-NOTA-C<sub>18</sub>, and <sup>64</sup>Cu-NOTA-UCNPs</i> .....	51
<b>Figure 13.</b> <i>Comparison of time activity curve of meanSUV between free <sup>64</sup>Cu , <sup>64</sup>Cu-NOTA- C<sub>18</sub>, and <sup>64</sup>Cu-NOTA-UCNPs in in vivo PET images</i> .....	53
<b>Figure 14.</b> <i>Evidence of hepatobiliary excretion in the collected feces using</i>	

*PET*.....55

**Figure 15.** *Evidence of hepatobiliary excretion in the collected feces using upconversion luminescence (ULI) imaging*.....56

**Figure 16.** *Evidence of urinary excretion using upconversion luminescence imaging (ULI)*.....57

**Figure 17.** *Observation of hepatobiliary excretion using TEM study*.....61

## List of Abbreviations

<i>Full name</i>	<i>Abbreviation</i>
nanoparticles	NPs
upconverting nanoparticles	UCNPs
micelle encapsulated <sup>64</sup> Cu-labeled upconverting nanoparticles	micelle encapsulated <sup>64</sup> Cu-NOTA-UCNPs
upconversion luminescence imaging	ULI
transmission electron microscopy	TEM
positron emission tomography	PET
mononuclear phagocyte system	MPS
near-infrared	NIR
dynamic light scattering	DLS
mean standardized uptake values	meanSUV
percentages of doses injected per gram of tissue	% ID/g

## Introduction

Although NPs have a huge potential as both diagnostic imaging and therapeutic agents, a majority of attempts for clinical translation have been blocked by unsolved biocompatibility issues. Small sized NPs infiltrate into organ, tissue, cellular, and protein level easily and exhibit high accumulation in variable organs. Indeed, delayed excretion and non-biodegradability of NPs have caused overt toxicity and tissue damage (1-5).

Markedly delayed excretion of variable NPs has been reported. First, cadmium is primarily utilized in the construction of particles known as quantum dots (QDs). The core of QDs is composed of toxic heavy metals, therefore, cytotoxicity is a definite concern for *in vivo* application (6, 7). Primary accumulation of QDs coated with 3-mercaptopropionic acid (MPA) in lungs and atriums of heart, and QDs705 in lungs was observed. Experiments demonstrated that QD MPA and QD polyethylene glycol (PEG) have both remained fluorescence in lungs after at least 24 hours post injection. Moreover, QDs MPA was seen to deposit mainly in liver, spleen, kidney and lymph nodes (in decreasing order of fluorescence), and in sites of blood supply of the skin, and muscles as well as of the brain. Moreover, researchers demonstrated that QDs are sequestered and not excreted with feces or urine (8). Second, East et al. investigated the 47-year-old woman who already had argyria due to silver toxicity. By using a radioactive tracer, the amount of silver following oral absorption was found to remain constant for up to 30 weeks (9). Matuk et al. found that orally administered silver nitrate caused

silver deposition in the eyes as granules that were still present 12 months after administration (10). And, Van der Zande et al. found that silver was still present in rat brain and testes 8 weeks post oral dosing of silver ions or silver NPs (15 and 20 nm) (11, 12). Third, metal oxide NPs can be composed of a variety of diverse materials. Some types of NPs, titanium dioxide (TiO<sub>2</sub>) NPs, are used in a variety of consumer products such as sunscreens, cosmetics, paints, and surface coatings as well as in the environmental decontamination of air, soil, and water. Such widespread use raises concern that TiO<sub>2</sub> NPs could pose a risk to both ecosystems and human beings. A previous study reported that chronic exposure to TiO<sub>2</sub> NPs induced significant inhibition of growth and reproduction in *Daphnia magna* (13) and induced neurotoxicity in the brain due to TiO<sub>2</sub> particles (rutile :80 nm, and anatase :155 nm), following nasal instillation exposure (500 µg/mouse, every other day, for a total of 30 days) (14). Also the pathological response associated with the pulmonary exposure to TiO<sub>2</sub> has been revealed by a number of investigators (15). Recently, it has been reported that the phagocytosis by macrophages was a significant factor causing the retention of TiO<sub>2</sub>-NPs mainly in liver and spleen, over 30 days in these tissues (16). Fourth, naked gold NPs without coatings can cause serious aggregation. Therefore, naked gold NPs with all sizes (5-100 nm) were severely accumulated in liver and spleen (17, 18). And gold NPs (18-nm) were completely removed from the blood and trapped predominantly in liver and spleen after 24 hours. However, a relatively small amount (0.5% of the injected dose [ID]) of gold NPs was excreted via the hepatobiliary system into the feces, but renal excretion was extremely low. In contrast, 1.4-nm gold NPs were excreted by

the kidneys as well as by the hepatobiliary system (urine: 8.6% ID, feces: 5% ID). The accumulation of 1.4-nm NPs in liver and spleen was significantly lower compared with that of the 18-nm NPs. No specific uptake in any organs could be observed, but significant amounts of the ID (3.7%) were circulated in the blood even at 24 hours post injection (19). Fifth, silica NPs without surface modification exhibited cytotoxic and genotoxic properties at high doses as well as interfered with cell cycle (20). Silica NPs after the tail vein injection in mice induced injuries of liver, spleen and lungs. Mononuclear phagocytic cells played an important role in the injury process (21). And colloidal silica was shown to induce red blood cells hemolysis and blood monocytes injury (22). Surface-modified silica NPs could be used for *in vivo* gene therapy (23) and labeling of human mesenchymal stem cells (24). However, little is known about the possible *in vivo* degradation processes of these particles and the toxicity of the resulting products which limit their biomedical applications .

The unwanted cytotoxicity and other side effects of NPs should be reduced because it is a prerequisite for medical application. Many reports demonstrated that NPs are persistently taken by the mononuclear phagocyte system (MPS) and induce tissue toxicity in liver and spleen (3, 25). On the other hand, by modifying surface characteristics, NPs could be excreted via hepatobiliary excretion pathway without overt tissue toxicity (26, 27). Therefore, it is critical to develop the biocompatible NPs that show favorable excretion property to minimize toxicity *in vivo*.

Micelle encapsulation method for hydrophilization of nanomaterials was

first described by Dubertret et al (28) and further refined by several groups (29-31). Recently, our group integrated the method and proposed one-step method under mild conditions to preserve ligand integrity to make functionally active multi-specific NPs. The NPs showed highly specific tumor targeting ability (32). However, biodistribution and excretion pattern of micelle encapsulated NPs have not been well evaluated since then.

The multifunctional NPs have been widely investigated for biomedical applications. The biocompatibility issue is one of the most significant parts for clinical translation. Of the relatively low cytotoxic NPs, the lanthanide ion-doped upconverting NP (UCNP) has been recognized as an emerging material in the area of nanomedicine. Thanks to its intrinsic capability that can emit visual light upon absorption of long wavelength near-infrared (NIR) photons, UCNPs have recently received much interest for the *in vivo* imaging application. Indeed, excitation by NIR may provide the superior advantages of autofluorescence-free nature (33), good penetration depth, and low photodamage in cells (34). Also, in the study recently reported by our group, UCNPs taken up by cancer cells were released out of cells through exocytosis within 24 hours. Meanwhile, HeLa cells treated with actin filaments inhibitors (cytochalasin D) before adding UCNPs showed perinuclear accumulation of UCNPs (34-38). Therefore, on the basis of previous results regarding initial exocytosis of UCNPs in the cell condition, I formulated the hypothesis that UCNP injected via systemic route would be rapidly excreted from the body.

Positron emission tomography (PET) has been considered as useful

imaging modality for biodistribution study with high sensitivity, depth penetration and capability of quantification (39)(40). Also, compared to fluorescence imaging probes, PET needs very low dose of radiopharmaceuticals to obtain an adequate image both in normal or pathological subjects. Therefore, it is biologically safe and non-toxic. The NOTA-chelated  $^{64}\text{Cu}$  ( $^{64}\text{Cu}$ -NOTA) with a relatively long half-life (762 min) is suitable to evaluate the biodistribution for 72 hours and has a water soluble characteristics enabling bioimaging application (41).

## **Purpose**

In the present study, I demonstrated the labeling method and characteristics of a bimodal imaging agent, micelle encapsulated  $^{64}\text{Cu}$ -NOTA-UCNP and showed the biodistribution and excretion pattern of the NPs using *in vivo* PET and ULI imaging. Moreover, I quantified the excretion of micelle encapsulated  $^{64}\text{Cu}$ -NOTA-UCNPs by PET and *ex vivo* method. And I finally explored the mechanism of hepatobiliary excretion by TEM study of liver tissue.

## Materials and Methods

### Chemicals

$\text{YCl}_3 \cdot 6\text{H}_2\text{O}$  (99.9%),  $\text{YbCl}_3 \cdot 6\text{H}_2\text{O}$  (99.9%),  $\text{ErCl}_3 \cdot 6\text{H}_2\text{O}$  (99.9%), oleic acid (technical grade, 90%), 1-octadecene (technical grade, 90%) and  $\text{NH}_4\text{F}$  (98.0%) were purchased from Aldrich. Sodium oleate was purchased from TCI. 1,2-distearoyl-sn-glycero-3-phosphoethanolamine-N-[methoxy(polyethylene glycol)-2000] (mPEG-2000 PE) was purchased from Avanti Polar Lipids, Inc. All reagents were used as received.

### Synthesis of hexagonal phase $\text{NaYF}_4:\text{Yb}^{3+}/\text{Er}^{3+}$ nanoparticles (UCNPs)

The hexagonal UCNPs were synthesized as described in a report by Li et al. (42). Y-oleate, Yb-oleate and Er-oleate complexes were prepared in the methods reported previously (43). Briefly, Y-oleate (0.78 mmol), Yb-oleate (0.2 mmol) and Er-oleate (0.02 mmol) complexes were mixed with oleic acid (10 mL) and 1-octadecene (15 mL) in a 100 mL three-neck round bottom flask. And the reaction mixture was heated to 100 °C under vacuum with stirring for 30 min to remove residual water and oxygen and then the solution was cooled as room temperature. Methanol solution (10 mL) containing NaOH (2.5 mmol) and  $\text{NH}_4\text{F}$  (4 mmol) was slowly added into the reaction vessel under argon. The reaction mixture was stirred for 30 min at 50 °C. Then temperature was gradually increased to 100 °C under vacuum with stirring for 30 min to remove methanol. Finally, the reaction mixture

was heated to 300 °C with a constant heating rate of 3.3 °C/min, and held at 300 °C for 1 hour under argon. The resulting solution was then cooled to room temperature. Concentration and composition of NPs were analyzed by inductively coupled plasma mass spectrometer (ICP-MS, ELAN 6100, Perkin- Elmer, Massachusetts, USA) at National Center for Inter-university Research Facilities (NCIRF, Seoul National University).

### **Synthesis of ligands conjugated with stearyl chains (NOTA-C<sub>18</sub>)**

1-(*p*-benzyl-1',4',7'-triazacyclononane-1',4',7'-triacetic acid)-3-octadecylthiourea (NOTA-C<sub>18</sub>) for <sup>64</sup>Cu labeling was synthesized by conjugating 2-(*p*-isothiocyanatobenzyl)-1,4,7-triazacyclononane-1,4,7-triacetic acid (SCN-Bn-NOTA) and stearylamine. SCN-Bn-NOTA (20 mg, 0.04 mmol) was dissolved in CHCl<sub>3</sub> (1 mL), and TEA (0.012 mL, 0.09 mmol) was added and stirred at room temperature. Stearylamine (14 mg, 0.05 mmol) was then added to the reaction mixture and stirred for 20 hours. The product was purified by the column chromatography and the structure was confirmed by mass spectroscopy. Yield: 26 mg (72%). MS-ESI, (M<sup>+</sup>-H<sup>+</sup>): 821.8. HRMS (M<sup>+</sup>H<sup>+</sup>): observed 720.4731, calculated 720.4734.

### **Encapsulation of UCNPs with amphiphiles**

The synthesis of water-soluble UCNPs was followed by the previous protocol (32). Polysorbate 60 was the commercially available (Sigma-Aldrich)

amphiphile used in this study. 4% (v/v) polysorbate 60 solution in distilled water (1 mL) was added to NOTA-C<sub>18</sub>. The mixture was then heated to 80°C at 20 min.

After the removal of hexane from UCNPs with inert gas, functionalized amphiphiles (2% [mol/mol] of polysorbate 60) were added. The mixture was sonicated for 80 min using VialTweeter at UIS250v at ~84.5 watt (Hielscher Ultrasonics GmbH, Teltow, Germany). The reaction mixtures containing UCNPs were applied to a Sephacryl S-400 column (Sigma-Aldrich) (6.7 × 150 mm) and eluted with distilled water to remove unbound polysorbate 60 and other amphiphiles. Fractions (1 mL) were collected and concentrated by ultrafiltration (Amicon Ultracel, 100-kDa cutoff; Millipore).

### **Stability Test**

The stabilities of micelle encapsulated <sup>64</sup>Cu-NOTA-UCNPs (0.37 MBq) in phosphate-buffered saline at room temperature and in human serum at 37 °C were determined by instant thin-layer chromatography-silica gel (ITLC-SG) plates (Pall Corp., U.S.A.) with 0.1 M citric acid at 0, 10, 30, 60 min and 2, 4, 8, 24 hours. The ITLC-SG strip was scanned using a TLC scanner (AR-2000, Bioscan, U.S.A.).

### **<sup>64</sup>Cu Radiolabeling**

<sup>64</sup>Cu was produced from cyclotron PETtrace 10 (GE healthcare, Sweden). NOTA-UCNPs (32 pmol, 10 μL) were mixed with <sup>64</sup>CuCl<sub>2</sub> (5-6 mCi/0.1 mL) in the presence of 1 M sodium acetate buffer (pH 5.6, 0.3 mL). Then the reaction mixture was incubated for 10 min at 45 °C. The labeling yield was determined by ITLC-SG

(1 × 10 cm strip) eluted with 0.1 M citric acid. The ITLC-SG strip was scanned using a TLC scanner. For the *in vivo* study, micelle encapsulated <sup>64</sup>Cu-NOTA-UCNPs were concentrated using an Amicon filtration system (Millipore).

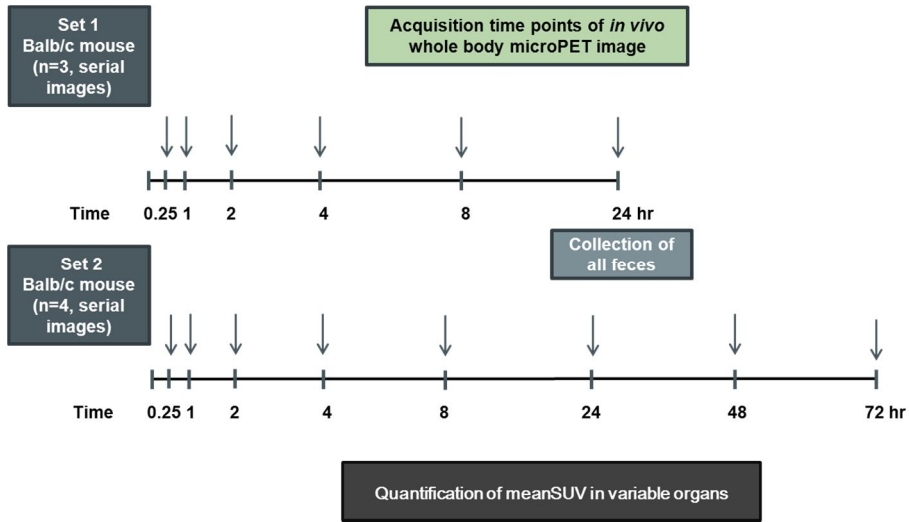
***In vivo* microPET imaging of micelle encapsulated <sup>64</sup>Cu-NOTA-UCNPs, <sup>64</sup>Cu-NOTA-C<sub>18</sub> and free <sup>64</sup>Cu injected mice**

Specific pathogen-free 6-week-old male BALB/c nude mice were obtained from SLC Inc. (Japan). All the animal experiments were performed after receiving approval from the Institutional Animal Care and Use Committee of the Clinical Research Institute at Seoul National University Hospital. In addition, the National Research Council guidelines for the care and use of laboratory animals (revised 1996) were observed throughout.

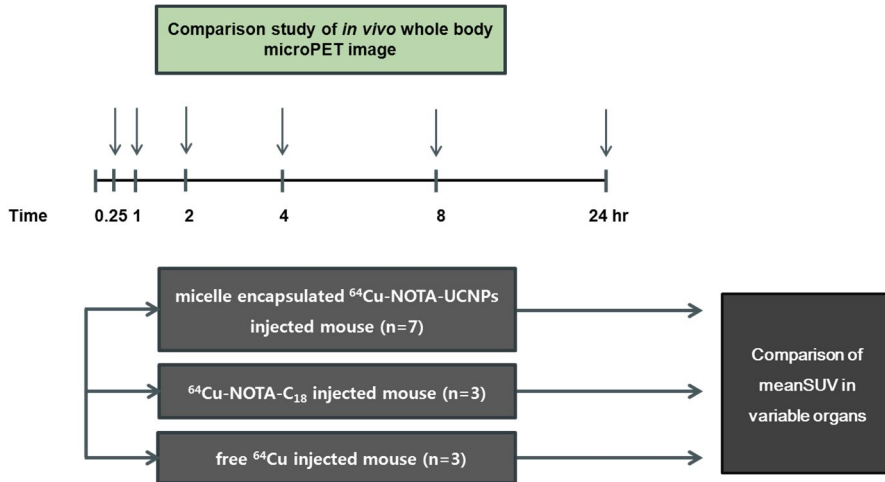
Using micelle encapsulated <sup>64</sup>Cu-NOTA-UCNPs and animal PET (GENISYS, Sofie Biosciences, Culver City, CA), the biodistribution study in BALB/c nude mice was evaluated. After micelle encapsulated <sup>64</sup>Cu-NOTA-UCNPs were injected to the tail vein of mice (weight = 24.1 ± 0.5 g, dose = 40 ± 0.6 μCi/50 μL), animal PET was performed to obtain serial time point images (0.25, 1, 2, 4, 8, and 24 hours, n = 3 / 0.25, 1, 2, 4, 8, 24, 48 and 72 hours, n = 4). Images were acquired for 15 minutes until 24 hours, and acquired for 30 and 60 minutes at 48hours, and 72 hours respectively. For the comparison study of free <sup>64</sup>Cu (n = 3), <sup>64</sup>Cu-NOTA-C<sub>18</sub> (n = 3) and micelle encapsulated <sup>64</sup>Cu-NOTA-UCNPs (n = 7), BALB/c nude mice were prepared. Dose of <sup>64</sup>Cu was 35 μCi/50 μL (19.9 g) and dose <sup>64</sup>Cu-NOTA-C<sub>18</sub> was 40 μCi/50 μL (18.6 g) by tail vein injection before PET

image obtaining. Dynamic whole-body PET images were obtained for 15 min in 20 frames ( $10 \times 60$  s). The images were obtained by 3-dimensional Fourier rebinning using a 2-dimensional ordered-subsets expectation maximization reconstruction algorithm with scatter, decay, and attenuation correction from raw framed sonograms. In each PET image, 3-dimensional regions of interest were drawn over major organs on whole-body axial images. Mean standardized uptake values (meanSUV) were obtained using PMOD software from reconstructed data. Animal PET was performed serially at 30 min, after injection under isoflurane inhalation anesthesia. After acquisition of 24 hours delayed PET image, mice were sacrificed. All liver and spleen were fixed in formaline solution. Feces and urine of mice after injection of micelle encapsulated  $^{64}\text{Cu}$ -NOTA-UCNPs were evaluated by PET image to confirm the excretion of micelle encapsulated  $^{64}\text{Cu}$ -NOTA-UCNPs. The biodistribution and microPET experiments were performed at Seoul National University Hospital, which is fully accredited by AAALAC International (2007, Association for Assessment and Accreditation of Laboratory Animal Care International).

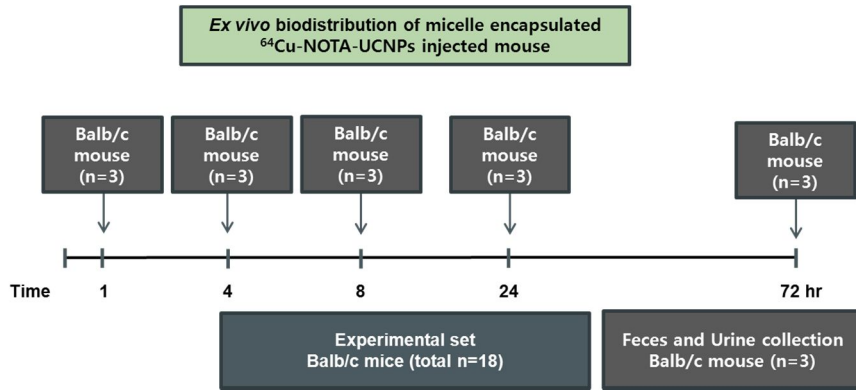
**a**



**b**



c



d

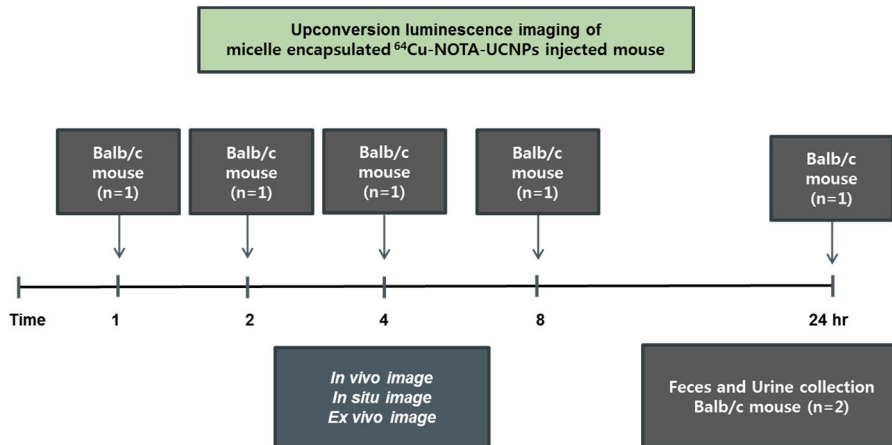


**Figure 1.**

Experimental design **a**, Biodistribution study using *in vivo* microPET after the injection of micelle encapsulated  $^{64}\text{Cu}$ -NOTA-UCNPs **b**, Comparison study of *in vivo* microPET between micelle encapsulated  $^{64}\text{Cu}$ -NOTA-UCNPs,  $^{64}\text{Cu}$ -NOTA- $\text{C}_{18}$  and free  $^{64}\text{Cu}$  injected mice **c**, *Ex vivo* biodistribution **d**, *In vivo*, *in situ*, and *ex vivo* upconversion luminescence imaging and TEM images

## **Biodistribution study using micelle encapsulated $^{64}\text{Cu}$ -NOTA-UCNPs and *ex vivo* method**

All mice used were male BALB/c mouse (4 ~ 5 weeks old) obtained from the breeding facility of the Seoul National University Hospital Biomedical Research Institute. Micelle encapsulated  $^{64}\text{Cu}$ -NOTA-UCNPs were injected into a male BALB /c mouse via the tail vein (weight =  $20.1 \pm 0.5$  g, dose =  $1 \mu\text{Ci}/100 \mu\text{L}$ ). The injected mice were sacrificed in serial time points (1, 4, 8, 24, and 72 hours, 3 mice for collection of feces and urine,  $n = 3$ , respectively, total  $n = 18$ ) of post-injection. Blood, liver, muscle, kidney, lung, heart, small intestine, large intestine, bone and other organs were excised, blotted and weighed, and then  $^{64}\text{Cu}$  radioactivity of each organ was counted by a gamma scintillation counter (DREAM r-10, Shinjin Medics Inc., South Korea). The results are expressed in percentages of doses injected per gram of tissue (% ID/g) and in percentages of doses injected per organ (% ID/organ).

## **Preparation of intraluminal feces, feces and urine smear section for upconverting luminescence imaging**

Whole large and small intestine of BALB/c nude mouse after 8 hours injection of UCNPs was sliced about 3 cm size and each resected intestine was put on the slide glass. For reducing penetration scattering of photoluminescence, I dissected intestinal lumen vertically in every 3 cm size intestine. The specimens were extended on the slide glass and was compressed by the other glass. Feces were collected for the serial time points. Individual feces were compressed and

enlarged by the slide glass for the better optical image. Spotty urine from mice after 30 min and 1 hour injection of UCNPs was collected and normal saline was mixed for the slide glass smear. Photoluminescence images of feces and urine were obtained, respectively.

### **Upconversion luminescence spectra of UCNPs**

In house optical imaging tool for *in vivo* UCNP imaging was used. The UCNP solutions were excited by 980-nm CW laser (SDL-980LM-500T, Shanghai Dream Lasers Technology) and the emission was collected at right angle by an optical fiber and detected by a CCD camera (PIXIS 400BR, Princeton Instruments) attached to a monochromator (HoloSpec f/1.8, Kaiser Optical Systems). It was composed of an inverted microscope (TE2000-U, Nikon), an NIR (980 nm) diode laser (P161-600-980A, EM4), and an electron multiplying CCD (EMCCD) camera (DV897DCS-BV, iXon, Andor Technology). The output of the 980 nm laser was reflected by a short-pass dichroic beam splitter (725dcspxr, Chroma Technology) and directed to the microscope objective (Plan Apo VC, 60X, NA 1.40, oil immersion, Nikon). The beam was focused on the back focal plane of the objective by a planoconvex lens (focal length 400 mm) resulting in the illumination area with diameter of ca. 60 mm. The typical power density of illumination was 300 W/cm<sup>2</sup> on the sample surface. The emission from the UCNPs in the visible range was collected by the same objective, passed through the dichroic beam splitter and a short-pass emission filter (ET700sp-2p, Chroma Technology), magnified further by a set of achromatic lenses outside the microscope, and finally imaged by the

EMCCD camera. The transmission range of the emission filter (400-700 nm) covers both the green (centered at 525 and 545 nm) and red (centered at 657 nm) emission bands from UCNPs. I also obtained bright field images of feces and urine samples using the same EMCCD camera and a lamp as the light source.

### **Acquisition of upconversion luminescence imaging**

The *in vivo* ULI in BALB/c nude mice was performed after tail vein injection of UCNPs (weight =  $24.1 \pm 0.5$  g, dose =  $158 \mu\text{g}/300 \mu\text{L}$ , total  $n = 7$ ). Before the image acquisition, peritoneal anesthesia in mice was performed. *In vivo* photoluminescence imaging was obtained as serial time points (1, 2, 4, 8, and 24 hours). For *in situ* image, nude mouse skin and peritoneum was exfoliated. After sacrifice, *ex vivo* image was performed. All images were acquired under the same experimental condition (980 nm laser power = 21 W (30 A),  $\sim 300 \text{ mW}/\text{cm}^2$ , EMCCD Gain = 250, exposure time = 10 s).

### **Acquisition of TEM**

TEM images were taken at an acceleration voltage of 80 keV (JEM-1400; Jeol). To obtain negative-stain TEM images of encapsulated UCNPs, UCNPs solutions were dropped onto a Formvar carbon-coated copper grid (SPI-Chem) and stained with saturated uranyl acetate solution. To observe hepatobiliary excretion, liver specimens were carefully selected. Liver tissue from UCNP injected mice was chopped and multiple pieces were selected including different 5 regions of both lobes of liver, 1 hour ( $n = 3$ ) and 24 hours ( $n = 4$ ) after injection.

### **Statistical analysis**

Data were calculated using the Student's *t*-test. Statistical significance was accepted at *P* values of  $< 0.05$ .

## Results

### *Part I. Characteristics of micelle encapsulated $^{64}\text{Cu}$ -NOTA-UCNPs*

#### *Synthesis of micelle encapsulated $^{64}\text{Cu}$ -NOTA-UCNPs*

The UCNPs were hexagonal  $\text{NaYF}_4:\text{Yb}^{3+}, \text{Er}^{3+}$  with a diameter of ca. 35 nm. Hydrophobic UCNPs were encapsulated by polysorbate 60 to transfer the hydrophobic UCNPs into aqueous phase. NOTA- $\text{C}_{18}$  was introduced as a ligand. Next,  $^{64}\text{CuCl}_2$  was added and  $^{64}\text{Cu}$ -NOTA-UCNPs were produced. The synthesis of water-soluble  $^{64}\text{Cu}$ -NOTA-UCNPs was followed by the previous protocol (32). The illustration of the whole labeling protocol was noted in Figure 2. UCNPs showed hexagonal shape on TEM, and were not changed after micelle encapsulation and radiolabeling (Fig. 3a). The UCNP solutions showed visible green light by 980-nm laser excitation (Fig. 3b).

#### *Purity, size and zeta potential*

The radiochemical purity of micelle encapsulated  $^{64}\text{Cu}$ -NOTA-UCNPs was 99%. The hydrodynamic size and zeta potential of UCNPs, and micelle encapsulated  $^{64}\text{Cu}$ -NOTA-UCNPs were  $34.10 \pm 6.40$  nm /  $-27.1 \pm 5.43$  mV and  $34.40 \pm 2.60$  nm /  $-6.63 \pm 6.31$  mV, respectively (Fig. 4).

### *Stability test*

Micelle encapsulated  $^{64}\text{Cu}$ -NOTA-UCNPs were stable for more than 24 hours in phosphate-buffered saline at room temperature (100%) and in human serum at 37 °C (75%) (Fig. 5).

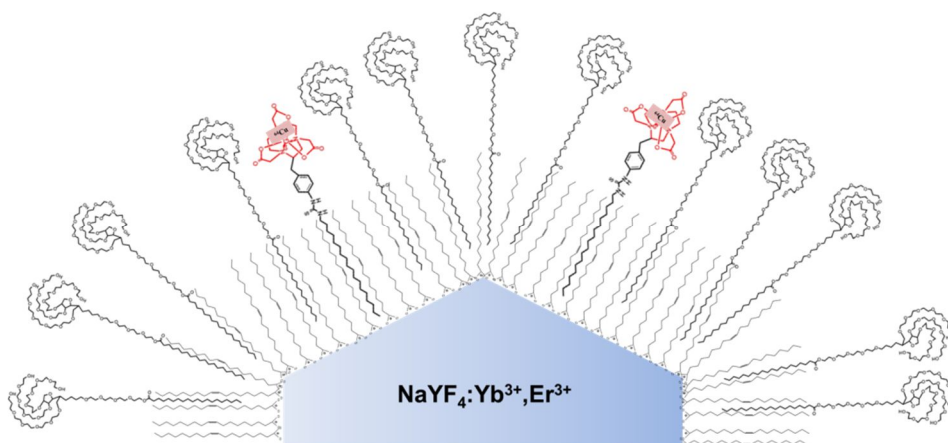


**Figure 2.**

Schematic illustration of micelle encapsulated  $^{64}\text{Cu}$ -NOTA-UCNP synthesis. Polysorbate 60 was used to transfer the hydrophobic UCNP into aqueous phase and NOTA- $\text{C}_{18}$  was used for the radiolabeling. Then,  $^{64}\text{Cu}$  was added and labeled with NOTA-UCNPs. Enlarged configuration of micelle encapsulated  $^{64}\text{Cu}$ -NOTA-UCNP was included. UCNP was encapsulated by polysorbate 60, NOTA- $\text{C}_{18}$ , oleic acid and  $^{64}\text{Cu}$ , which was micelle encapsulated  $^{64}\text{Cu}$ -NOTA-UCNP.

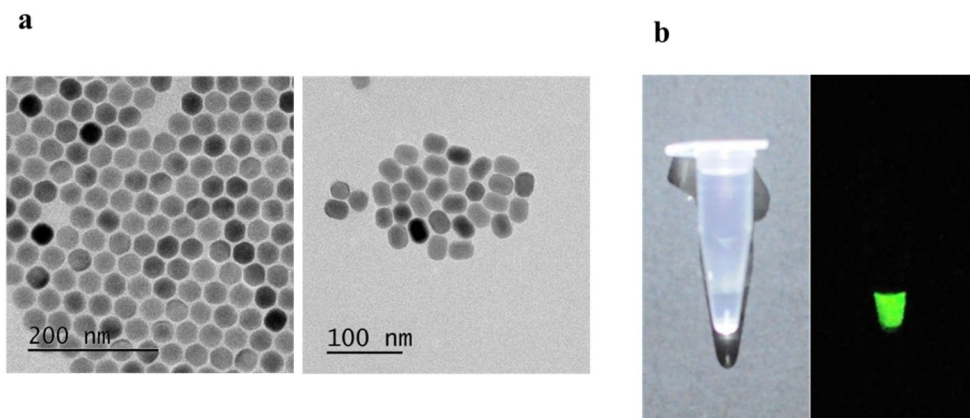


**Figure 3.**

TEM images of UCNPs and micelle encapsulated  $^{64}\text{Cu}$ -NOTA-UCNP. **a**, UCNPs showed hexagonal shape (left) on TEM, and were not changed after micelle encapsulation and radiolabeling (right). **b**, The UCNP solutions showed visible green light by 980-nm laser excitation.

Radiochemical purity : 99%

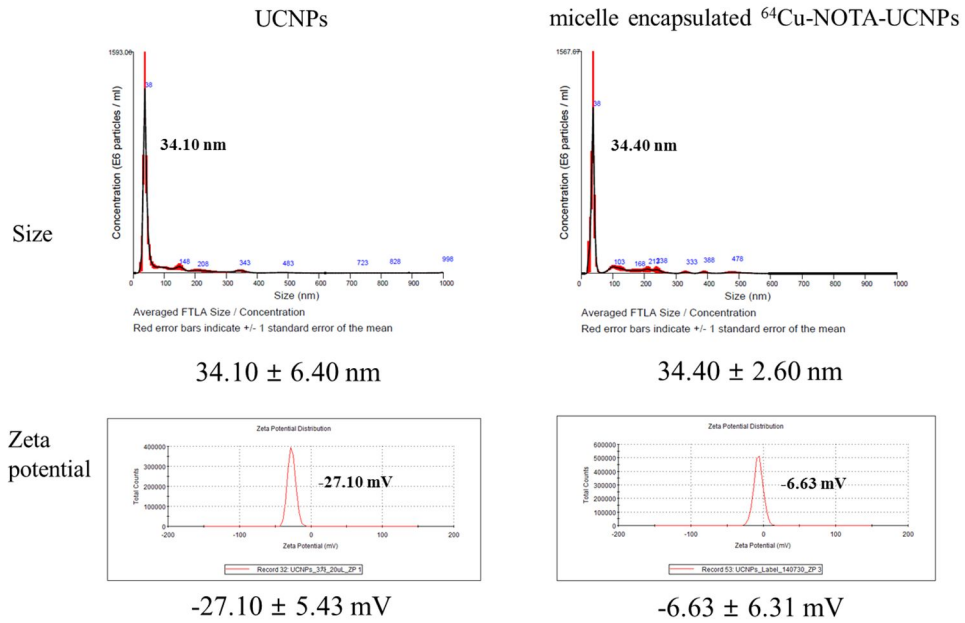


**Figure 4.**

The hydrodynamic size and zeta potential of UCNPs, and micelle encapsulated <sup>64</sup>Cu-NOTA-UCNPs. The size and zeta potential of UCNPs, and micelle encapsulated <sup>64</sup>Cu-NOTA-UCNPs were 34.10 ± 6.40 nm / -27.1 ± 5.43 mV and 34.40 ± 2.60 nm / -6.63 ± 6.31 mV, respectively.

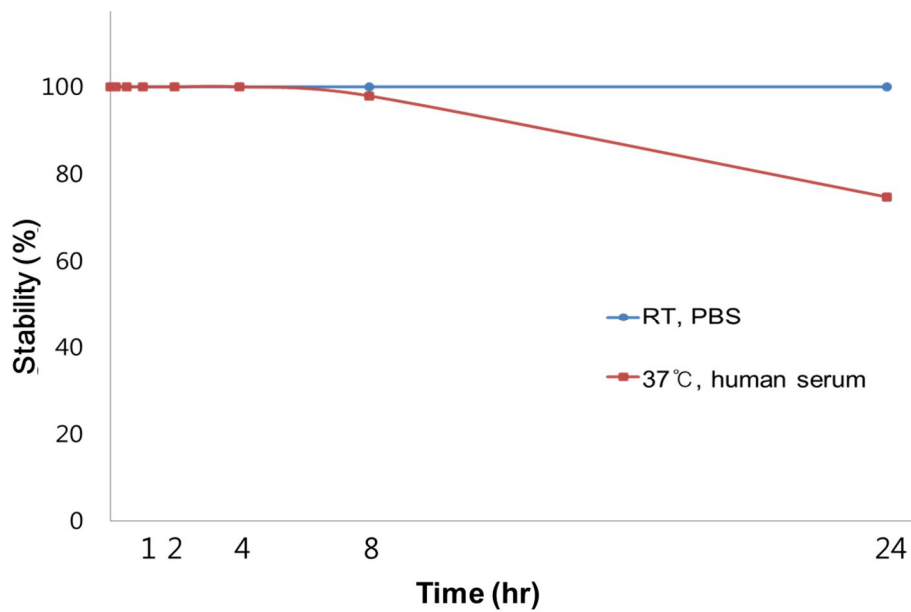


**Figure 5.**

Stability test of micelle encapsulated  $^{64}\text{Cu}$ -NOTA-UCNPs. Micelle encapsulated  $^{64}\text{Cu}$ -NOTA-UCNPs were stable for 24 hours in phosphate-buffered saline at room temperature (100%) and in human serum at 37 °C (75%)

***Part II. Multimodal imaging and quantification of hepatobiliary excretion of micelle encapsulated <sup>64</sup>Cu-NOTA-UCNPs***

*In vivo biodistribution study of whole body microPET imaging*

*In vivo* PET images were obtained at serial time points after intravenous injection of micelle encapsulated <sup>64</sup>Cu-NOTA-UCNPs. I could obtain serial PET images of favorable image quality in a mouse with a very small amount of NPs (12 µg / mouse) until 72 hour after injection. Initially, the tracer uptake was shown primarily in liver and lung at 0.25 hour PET image. At 1 hour delay image, uptake in lung was not shown. However, hepatic uptake had persisted until 8 hour delay image. At 1 hour delay image, the intestinal uptake was found and the extent of intestinal uptake was further enlarged along intestine at 2, 4 and 8 hour delay images. However, hepatic uptake was markedly decreased at 24 hour delay image compared to 8 hour delay image, and further decreased at 72 hour image (Fig. 6).

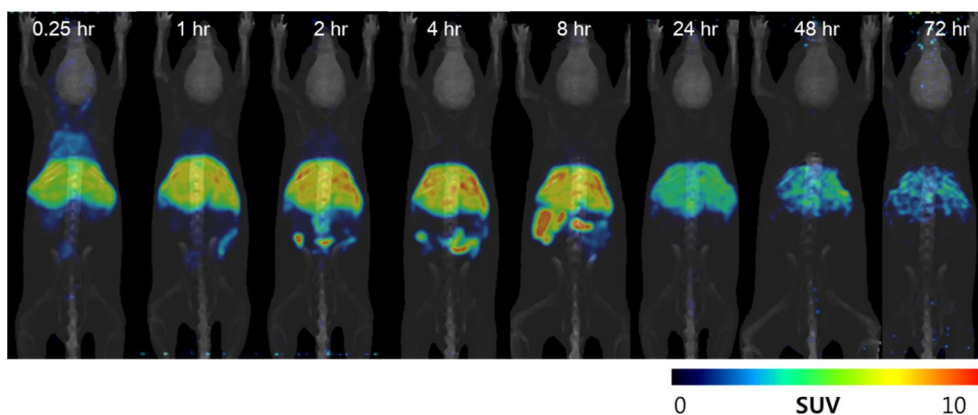


**Figure 6.**

*In vivo* whole body microPET imaging. Decay-corrected MIP (Maximum Intensity Projection) images in BALB/c nude mice at different time points after intravenous injection of micelle encapsulated  $^{64}\text{Cu}$ -NOTA-UCNPs (0.25, 1, 2, 4, 8, 24, 48, and 72 hours) were shown. Hepatic uptake was increased until 2 hours delay image, and then decreased serially. The blood pool activity was visualized in heart, lung and both kidneys at 0.25 hour image. Excretion to the intestine was noted after 1 hour, which showed the segmental uptake along intestine. Linearly intestinal uptake was seen until 8 hours and was decreased after 24 hours post- injection.

### *Quantification of in vivo whole body microPET imaging*

The serial PET images indicated that micelle encapsulated  $^{64}\text{Cu}$ -NOTA-UCNPs were excreted by hepatobiliary system after 1 hour post-injection. The excretion pattern could be quantified by region of interest analysis using serial PET images (Fig. 7). The meanSUV  $\pm$  SD of liver uptake was  $4.12 \pm 0.59$  at 0.25 hour,  $4.80 \pm 1.14$  at 1 hour,  $5.18 \pm 0.97$  at 2 hours,  $5.07 \pm 0.91$  at 4 hours,  $4.65 \pm 0.71$  at 8 hours,  $3.15 \pm 0.59$  at 24 hours,  $2.78 \pm 0.55$  at 48 hours, and  $2.14 \pm 0.70$  at 72 hours. Initially, liver uptake was increased in 17% at 1 hour, 27% at 2 hours, 23% at 4 hours, and 13% at 8 hours, compared with 0.25 hour scan. However, the meanSUV of liver uptake was markedly decreased in 59% at 72 hours, compared with 2 hour scan. Meanwhile, the meanSUV  $\pm$  SD of intestine was  $0.57 \pm 0.14$  at 0.25 hour,  $0.88 \pm 0.24$  at 1 hour,  $1.54 \pm 0.59$  at 2 hours,  $1.94 \pm 0.92$  at 4 hours,  $2.68 \pm 1.06$  at 8 hours,  $0.61 \pm 0.24$  at 24 hours,  $0.38 \pm 0.13$  at 48 hours, and  $0.29 \pm 0.11$  at 72 hours. The peak excretion to intestine was shown at 8 hours.

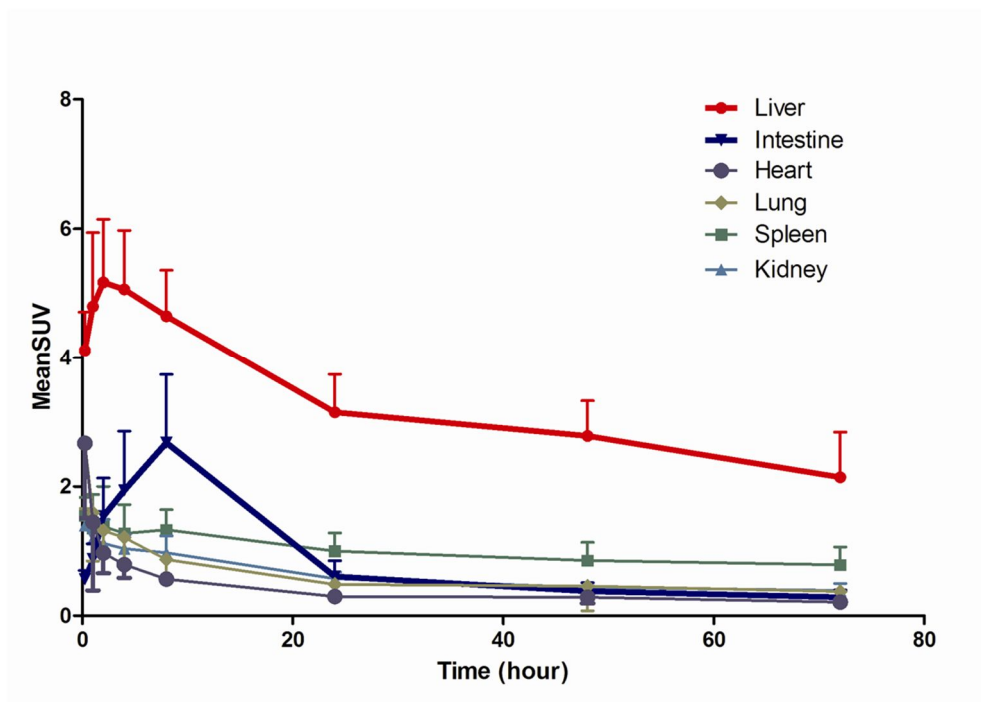


**Figure 7.**

Quantification of *in vivo* whole body microPET imaging. Quantitative *in vivo* PET image in mice after intravenous injection of  $50 \pm 0.6 \mu\text{Ci}$  (1.85 MBq) micelle encapsulated  $^{64}\text{Cu}$ -NOTA-UCNPs was analyzed. Data at serial time points (0.25, 1, 2, 4, 8, 24, 48, 72 hours) were obtained. Data ( $n = 7$ , until 8 hours,  $n = 4$  at 24, 48, 72 hours after injection) were expressed as mean  $\pm$  SD (meanSUV).

### *Ex vivo biodistribution study and quantification*

The *ex vivo* biodistribution data showed consistent results with PET images that the concentration of micelle encapsulated  $^{64}\text{Cu}$ -NOTA-UCNPs in liver was decreased persistently until 72 hours (Fig. 8). Early wash out pattern was observed in heart and lung. According to % ID per organ analysis, the percentage  $\pm$  SD of liver was  $45.04 \pm 2.13$  at 1 hour,  $43.64 \pm 1.71$  at 4 hours,  $32.14 \pm 0.48$  at 8 hours,  $13.16 \pm 0.62$  at 24 hours, and  $7.34 \pm 0.29$  at 72 hours, respectively. Therefore, 83.7 % of the initial hepatic radioactivity was excreted at 72 hours after injection. Meanwhile, the concentration of micelle encapsulated  $^{64}\text{Cu}$ -NOTA-UCNPs in intestine was sequentially increased in small intestine first and then large intestine until 8 hours and was decreased at 24 hours probably due to the expulsion of feces (Fig. 9). Collected feces and urine in *ex vivo* biodistribution consisted of  $40.9 \pm 3.3$  % ID and  $1.1 \pm 0.6$  % ID at 24 hours post-injection, respectively. The percentage of large intestine and small intestine  $\pm$  SD was  $0.81 \pm 0.04$  and  $7.42 \pm 0.30$  at 1 hour,  $9.62 \pm 1.74$  and  $10.54 \pm 1.48$  at 4 hours,  $19.64 \pm 1.12$  and  $8.02 \pm 0.36$  at 8 hours,  $2.95 \pm 0.97$  and  $2.78 \pm 0.06$  at 24 hours, and  $0.91 \pm 0.08$  and  $1.22 \pm 0.10$  at 72 hours, respectively.

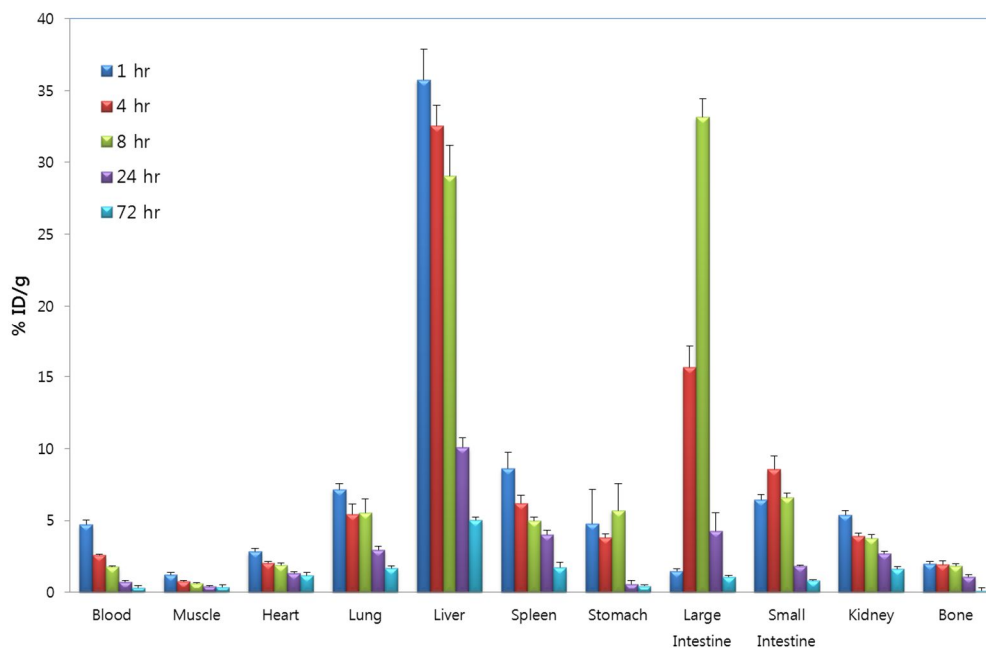


**Figure 8.**

Quantification of *ex vivo* biodistribution study. *Ex vivo* biodistribution in mice after intravenous injection of 1  $\mu\text{Ci}$  (37 kBq) micelle encapsulated  $^{64}\text{Cu}$ -NOTA-UCNPs was analyzed. Data ( $n = 3$ ) were expressed as mean  $\pm$  SD, indicating the percentage administered activity (injected dose) per total gram of tissue (% ID/g). The radioactivity of liver had been increased until 8 hours, but markedly decreased at 24 hours. Further decreased radioactivity of liver was observed at 72 hours. The radioactivity of intestine had been increased until 8 hours and decreased at 24 hours.

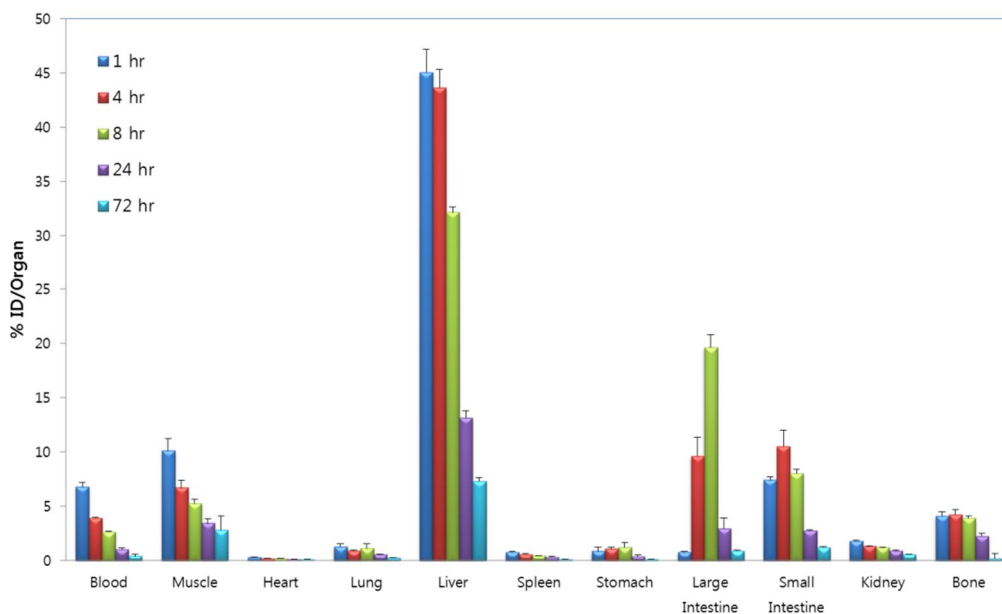


**Figure 9.**

Quantification of *ex vivo* biodistribution study according to organs. *Ex vivo* biodistribution in mice after intravenous injection of 1  $\mu\text{Ci}$  (37 kBq) micelle encapsulated  $^{64}\text{Cu}$ -NOTA-UCNPs was analyzed. Data ( $n = 3$ ) were expressed as mean  $\pm$  SD, indicating the percentage administered activity (injected dose) per organ (% ID/organ). Blood pool showed early wash out pattern. The radioactivity of liver was markedly decreased after 24 hours. Large and small intestine showed gradually increased uptake until 8 hours. The decreased radioactivity was owing to expulsion of feces from bowel and further decreased radioactivity was observed after 24 hours.

*In vivo, in situ and ex vivo upconversion luminescence imaging*

Luminescence images of micelle encapsulated  $^{64}\text{Cu}$ -NOTA-UCNPs at serial time points were done. Injection dose was escalated from 40  $\mu\text{g}/\text{mouse}$ , and to the dose of 158  $\mu\text{g}/\text{mouse}$ , I could obtain a sufficient signal for *in vivo* luminescent imaging which was 13 times higher amount than that for the dose of PET imaging (12  $\mu\text{g}/\text{mouse}$ ). In *in vivo* and *in situ* luminescence imaging, liver uptake had been decreased as further delayed time points (Fig. 10). This more rapid disappearance of liver luminescence signal than PET signal is probably due to limited depth penetration of luminescence imaging, because UCNPs would go into the deeper level of liver tissue for biliary excretion. In 1 hour post-injection *ex vivo* image, liver, spleen and lung showed the positive signal which was consistent with PET image (Fig. 11a). The intestinal uptake was not well-visualized in *in vivo* image, but after extraction and exposure of intestinal lumen, UCNP signal was clearly detected (Fig. 11b). In accordance with the *in vivo* PET images and *ex vivo* biodistribution study, the segmental or linear uptake along the intestinal lumen was well-visualized until 8 hours after injection, suggesting hepatobiliary excretion of UCNPs.

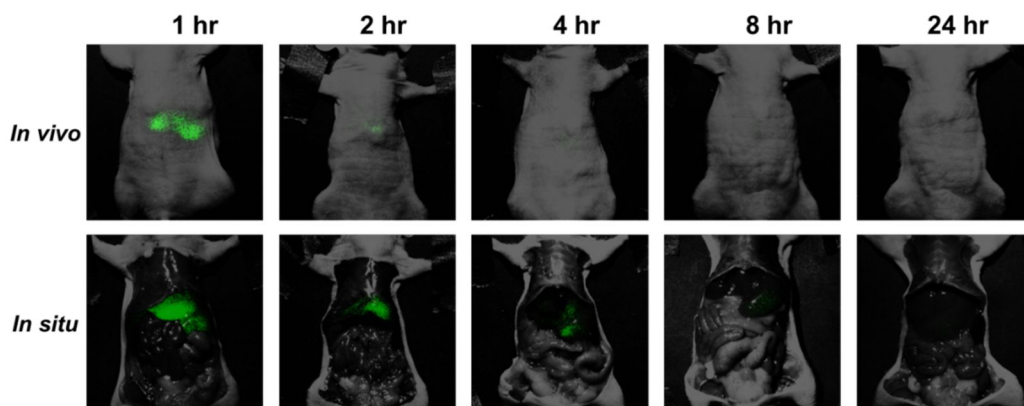
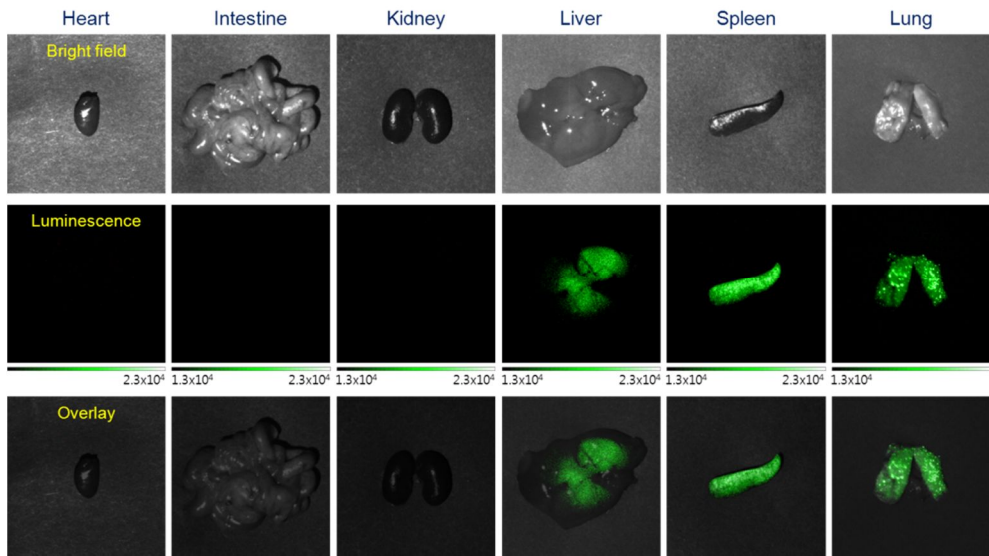


**Figure 10.**

*In vivo* and *in situ* upconversion luminescence imaging. *In vivo* and *in situ* images at different time points (1, 2, 4, 8, and 24 hours) after injection of micelle encapsulated  $^{64}\text{Cu}$ -NOTA-UCNPs were represented. *In vivo* liver uptake was markedly decreased at 2 hours. *In situ* image after the removal of peritoneum showed better visualization of liver and spleen. This finding was due to the limited penetration depth of UCNPs. Other organs showed no definite luminescence in *in vivo* and *in situ* images. All images were acquired under the same experimental condition (980 nm laser power = 21 W (30 A),  $\sim 300 \text{ mW/cm}^2$ , EMCCD Gain = 250, exposure time = 10 s).

**a**



**b**

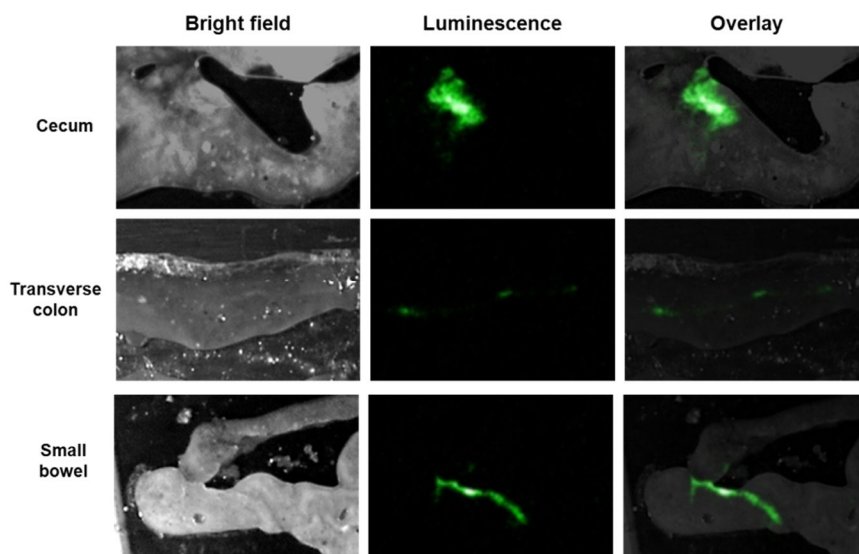


**Figure 11.**

*Ex vivo* upconversion luminescence imaging. **a**, *Ex vivo* upconversion luminescence image at 1 hour image showed the increased uptake in lung, liver and spleen. Upper column was bright field images of each organ, and middle column was luminescence images, and lower column was overlay images both bright field and luminescence. **b**, Multifocal luminescence signals along the lumen of intestine were manifested. Luminescence images of cecum, transverse colon and small bowel represented the flow of UCNPs due to peristalsis. All images were acquired under the same experimental condition (980 nm laser power = 21 W (30 A), ~300 mW/cm<sup>2</sup>, EMCCD Gain = 250, exposure time = 10 s).

***Part III. Evidence of hepatobiliary excretion of micelle encapsulated <sup>64</sup>Cu-NOTA-UCNPs***

*Comparison of in vivo PET images using free <sup>64</sup>Cu , <sup>64</sup>Cu-NOTA- C<sub>18</sub>, and <sup>64</sup>Cu-NOTA-UCNPs*

PET images for free <sup>64</sup>Cu (n = 3) or <sup>64</sup>Cu-NOTA- C<sub>18</sub> (n = 3) were acquired to verify the possibility of the detachment of free <sup>64</sup>Cu or <sup>64</sup>Cu-NOTA- C<sub>18</sub> from the injected micelle encapsulated <sup>64</sup>Cu-NOTA-UCNPs. Free <sup>64</sup>Cu or <sup>64</sup>Cu-NOTA- C<sub>18</sub> showed different biodistribution with micelle encapsulated <sup>64</sup>Cu-NOTA-UCNPs *in vivo* PET image (Fig. 12). Only <sup>64</sup>Cu-NOTA-C<sub>18</sub> showed initial high bladder uptake at 0.25 hour image indicating rapid renal excretion, contrary to the minimal bladder uptake in mice with micelle encapsulated <sup>64</sup>Cu-NOTA-UCNPs. According to the quantitative comparison, the uptake of <sup>64</sup>Cu-NOTA-C<sub>18</sub> and micelle encapsulated <sup>64</sup>Cu-NOTA-UCNPs in heart and lungs was cleared. However, free <sup>64</sup>Cu in blood pool has persisted until 24 hours after injection, probably due to recirculation of the copper ion. Both micelle encapsulated <sup>64</sup>Cu-NOTA-UCNPs and <sup>64</sup>Cu-NOTA-C<sub>18</sub> showed the initial higher hepatic uptake and faster excretion than free <sup>64</sup>Cu (Fig. 13). Thus, it is not likely that free <sup>64</sup>Cu or <sup>64</sup>Cu-NOTA- C<sub>18</sub> is detached from micelle encapsulated <sup>64</sup>Cu-NOTA-UCNPs *in vivo*, considering the differences of biodistribution.

Of mice injected with free <sup>64</sup>Cu, the meanSUV ± SD of liver uptake was

3.56 ± 0.15 at 0.25 hour, 4.54 ± 2.26 at 1 hour, 4.67 ± 0.51 at 2 hours, 4.85 ± 0.46 at 4 hours, 5.18 ± 0.33 at 8 hours, and 4.04 ± 0.49 at 24 hours. The meanSUV ± SD of intestinal uptake was 1.05 ± 0.17 at 0.25 hour, 1.25 ± 0.46 at 1 hour, 1.39 ± 0.58 at 2 hours, 1.61 ± 0.50 at 4 hours, 1.96 ± 0.96 at 8 hours, and 1.20 ± 0.53 at 24 hours. The meanSUV ± SD of heart was 0.86 ± 0.06 at 0.25 hour, 0.67 ± 0.22 at 1 hour, 0.65 ± 0.19 at 2 hours, 0.63 ± 0.13 at 4 hours, 0.74 ± 0.25 at 8 hours, and 0.82 ± 0.41 at 24 hours. The meanSUV ± SD of lung was 1.01 ± 0.30 at 0.25 hour, 1.00 ± 0.17 at 1 hour, 0.96 ± 0.25 at 2 hours, 0.99 ± 0.04 at 4 hours, 1.01 ± 0.15 at 8 hours, and 0.86 ± 0.28 at 24 hours.

Meanwhile, of mice injected with <sup>64</sup>Cu-NOTA-C<sub>18</sub>, the meanSUV ± SD of liver was 3.56 ± 0.23 at 0.25 hour, 4.33 ± 0.34 at 1 hour, 5.02 ± 0.80 at 2 hours, 4.06 ± 0.37 at 4 hours, 3.02 ± 0.08 at 8 hours, and 1.37 ± 0.12 at 24 hours. The meanSUV ± SD of intestine was 0.80 ± 0.36 at 0.25 hour, 0.94 ± 0.13 at 1 hour, 1.29 ± 0.16 at 2 hours, 1.73 ± 0.57 at 4 hours, 1.54 ± 0.19 at 8 hours, and 0.59 ± 0.31 at 24 hours. The meanSUV ± SD of heart was 2.48 ± 0.84 at 0.25 hour, 0.84 ± 0.03 at 1 hour, 0.76 ± 0.21 at 2 hours, 0.54 ± 0.13 at 4 hours, 0.44 ± 0.10 at 8 hours, and 0.19 ± 0.04 at 24 hours. The meanSUV ± SD of lung was 2.38 ± 0.30 at 0.25 hour, 1.39 ± 0.33 at 1 hour, 0.91 ± 0.31 at 2 hours, 0.91 ± 0.31 at 4 hours, 0.52 ± 0.17 at 8 hours, and 0.28 ± 0.07 at 24 hours.

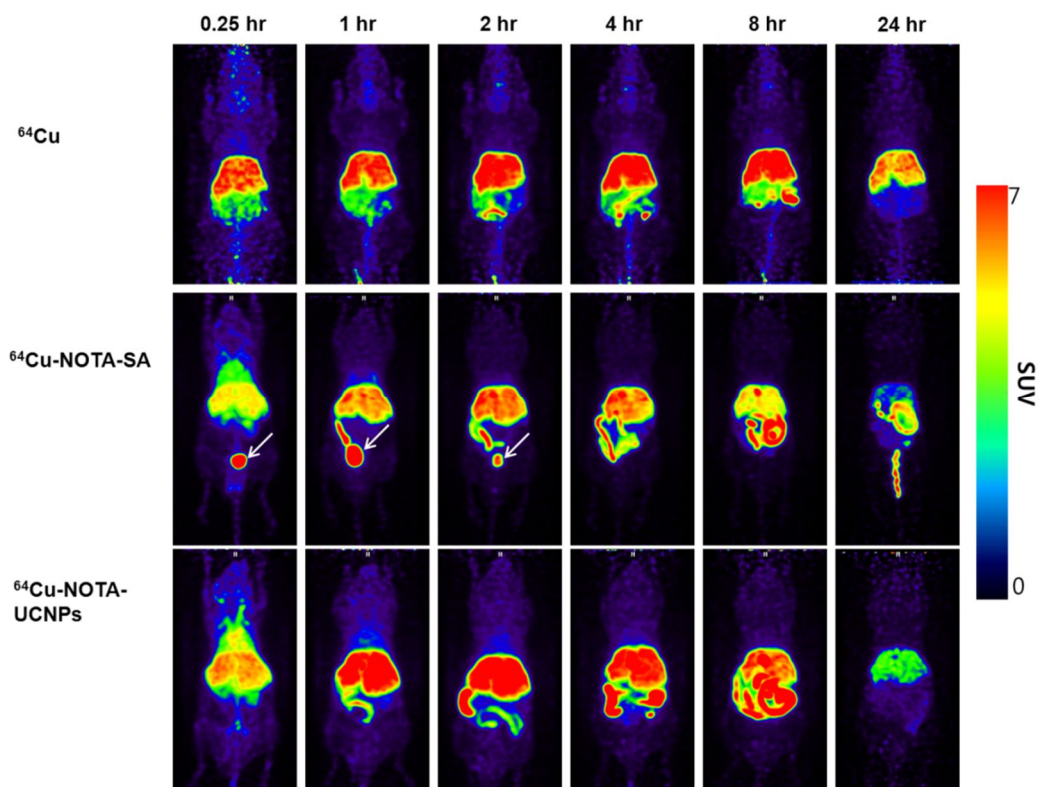


**Figure 12.**

Comparison of *in vivo* PET images using free  $^{64}\text{Cu}$ ,  $^{64}\text{Cu}$ -NOTA- $\text{C}_{18}$  (SA), and micelle encapsulated  $^{64}\text{Cu}$ -NOTA-UCNPs. Decay-corrected MIP PET images in BALB/c nude mice at different time points after about  $50 \mu\text{Ci}$  ( $1.85 \text{ MBq}$ ) intravenous injection of free  $^{64}\text{Cu}$ ,  $^{64}\text{Cu}$ -NOTA- $\text{C}_{18}$  and micelle encapsulated  $^{64}\text{Cu}$ -NOTA-UCNPs, respectively.

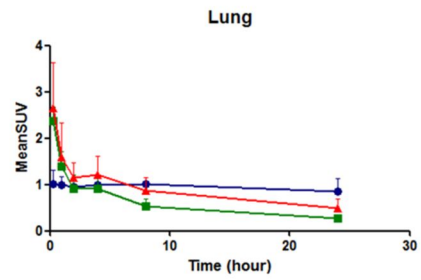
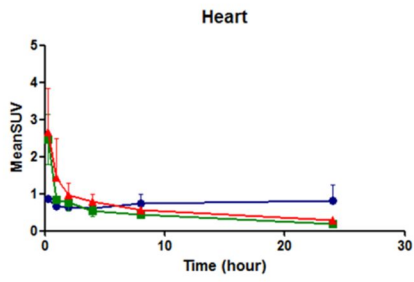
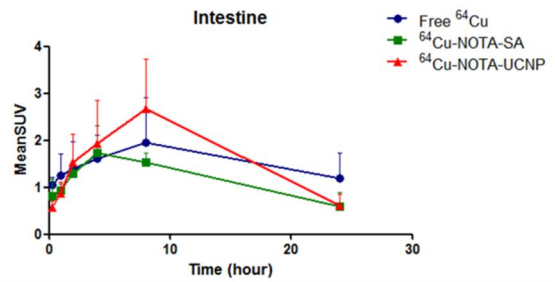
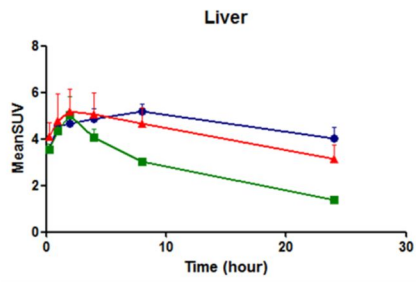


**Figure 13.**

Comparison of time activity curve of meanSUV between free  $^{64}\text{Cu}$ ,  $^{64}\text{Cu}$ -NOTA- $\text{C}_{18}$  (SA), and micelle encapsulated  $^{64}\text{Cu}$ -NOTA-UCNPs in *in vivo* PET images. In *in vivo* PET, uptake in liver was higher in micelle encapsulated  $^{64}\text{Cu}$ -NOTA-UCNPs injected mouse than free  $^{64}\text{Cu}$  or  $^{64}\text{Cu}$ -NOTA- $\text{C}_{18}$  injected mice at each time point. Intestinal uptake in micelle encapsulated  $^{64}\text{Cu}$ -NOTA-UCNPs injected mouse was higher at 2, 4, 8 hour delay PET images than free  $^{64}\text{Cu}$  or  $^{64}\text{Cu}$ -NOTA- $\text{C}_{18}$  injected mice. Uptake in heart and lung was cleared faster in free  $^{64}\text{Cu}$  and  $^{64}\text{Cu}$ -NOTA- $\text{C}_{18}$  injected mice than micelle encapsulated  $^{64}\text{Cu}$ -NOTA-UCNPs injected mouse.

*PET and upconversion luminescence images and ex vivo method of feces and urine*

To further support hepatobiliary excretion of the UNCPS, I collected feces and urine until 24 hours. Total % ID of *ex vivo* method in collected feces and urine was  $40.9 \pm 3.3$  and  $1.1 \pm 0.6$  %, respectively until 24 hours. Also intense PET signal was observed in most of feces samples (Fig. 14). The radioactivity of excreted feces from mice after injection of micelle encapsulated  $^{64}\text{Cu}$ -NOTA-UNCPS was significantly higher than that of excreted feces from control mouse ( $P < 0.05$ ). In addition, UCNP luminescence signal was observed in all collected feces after 4 hour post-injection confirming that UCNP was excreted via feces. Also in microscopic ULI, multiple scattered UCNP in feces showed the characteristic UCNP signals (Fig. 15). Urinary excretion of UCNP was also confirmed by luminescence images from urine sample, showing that spotty bright signal in tube 30 minutes and 1 hour after injection (Fig. 16). It was proven to be UNCPS by two different emission peaks from NPs in collected urine which were original upconversion luminescence characteristic of UCNP.

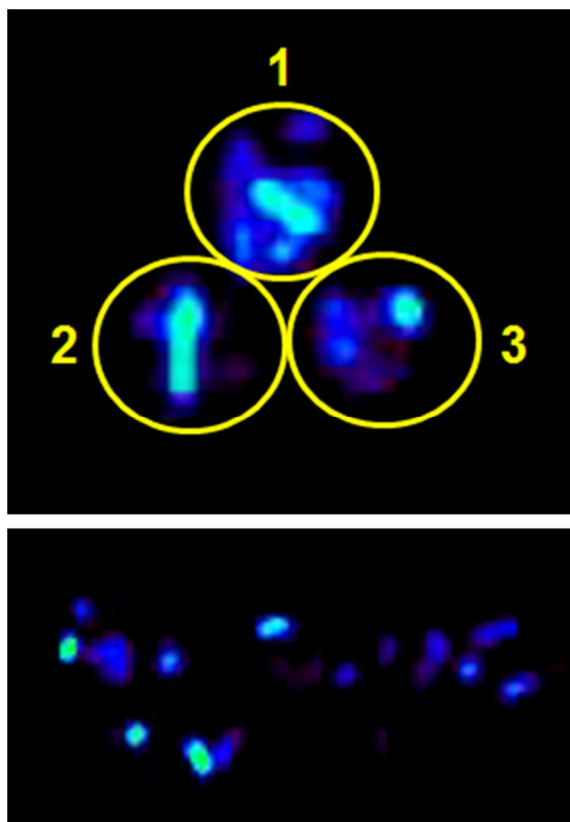


**Figure 14.**

Evidence of hepatobiliary excretion in collected feces using PET. PET images showed increased uptake in collected feces. Collected all feces (n=3) for 24 hours showed heterogeneously increased uptake. The  $\text{cpm} \pm \text{SD}$  of excreted feces of mice after injection of micelle encapsulated  $^{64}\text{Cu}$ -NOTA-UCNPs was  $1,014,622 \pm 213,497$  by gamma counter. The  $\text{cpm}$  of feces from mice with micelle encapsulated  $^{64}\text{Cu}$ -NOTA-UCNPs was significantly higher than that of feces from control mouse ( $P < 0.05$ ).

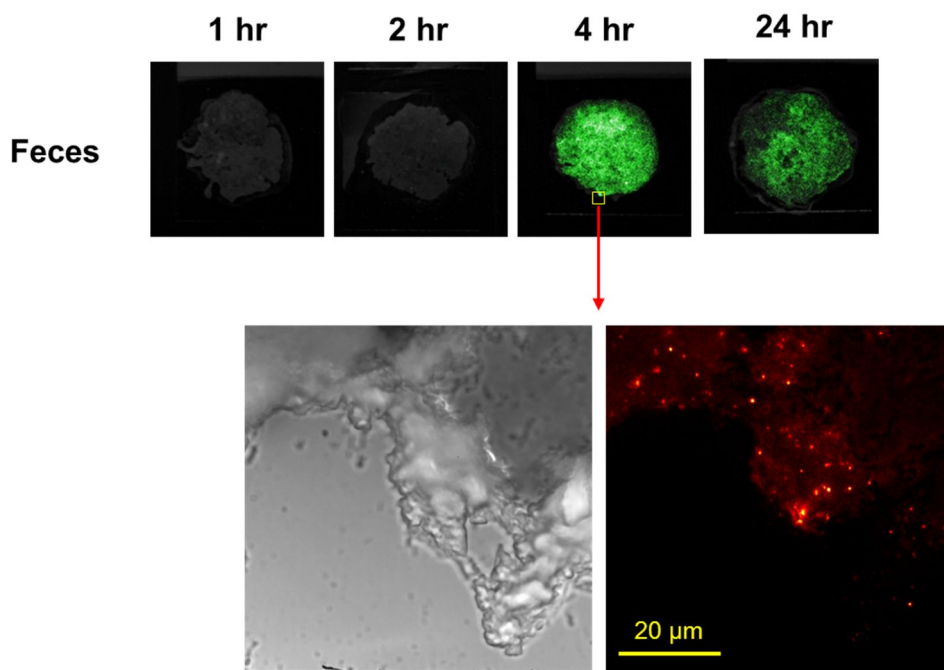


**Figure 15.**

Evidence of hepatobiliary excretion in collected feces using upconversion luminescence imaging according to serial time points. Microscopic image showed multiple and scattered UCNPs. The signal intensity was dominant in green (525-560 nm) and red (630-725 nm) light corresponding to the characteristics of UCNP signals.

## UCNPs in urine

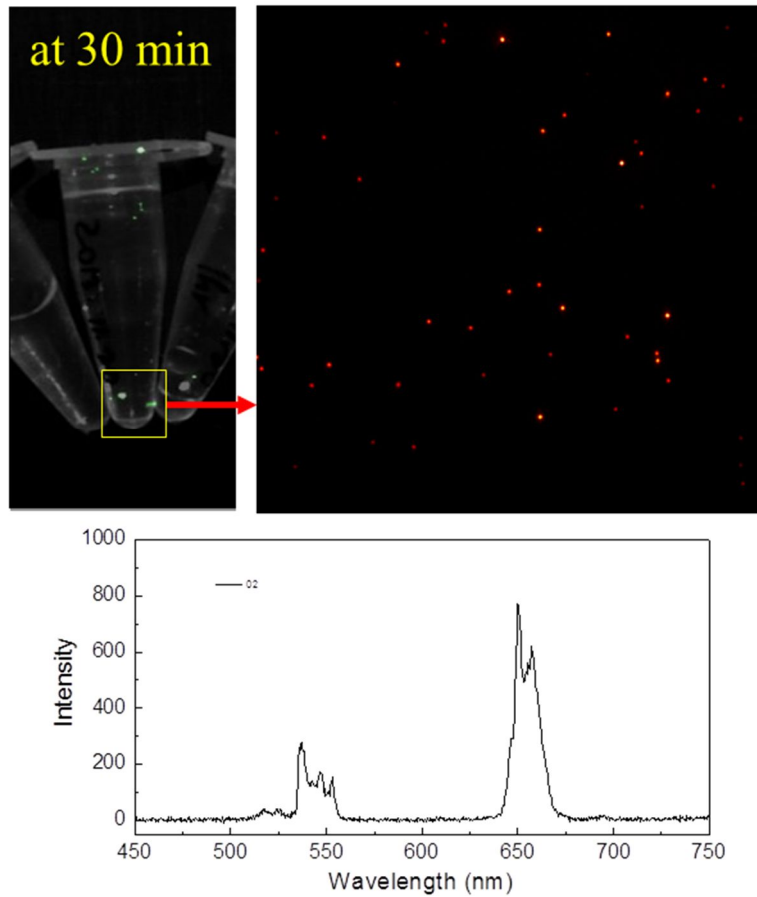
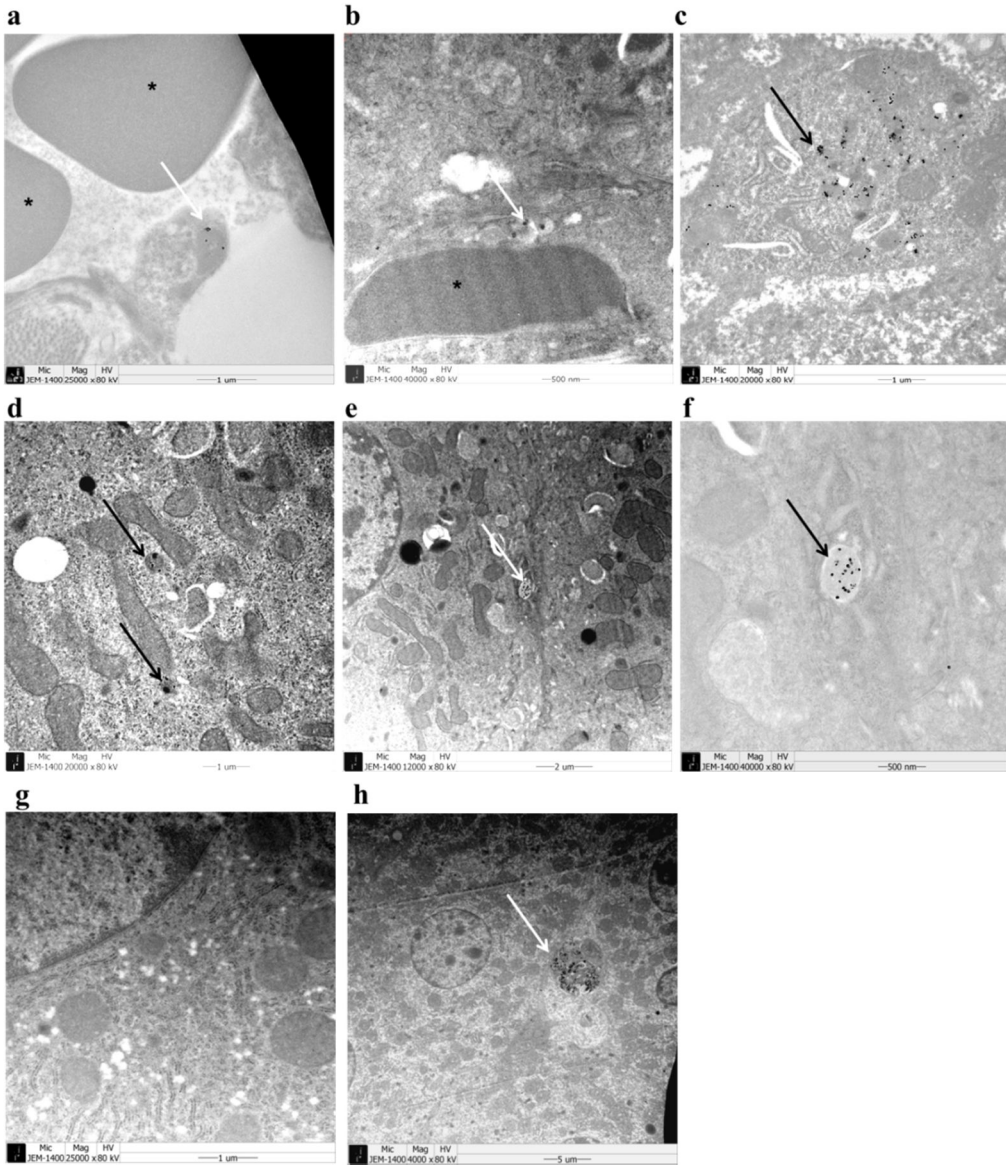


**Figure 16.**

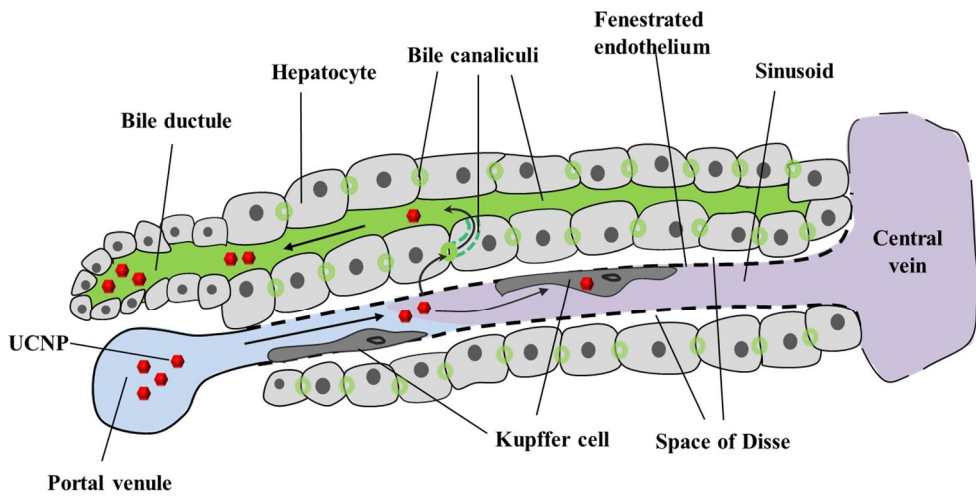
Evidence of urinary excretion using upconversion luminescence imaging. Upconversion luminescence imaging of collected urine at 30 minutes was obtained. Several spots with luminescence were observed inside of tube. Enlarged image shows multiple single UCNPs. The signal intensity was dominant in green (525-560 nm) and red (630-725 nm) light.

### *TEM study of hepatobiliary excretion*

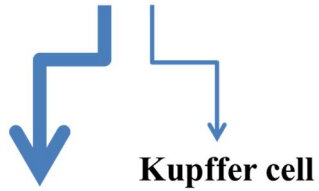
TEM study was done using liver section of mice sacrificed at 1 hour and 24 hours after injection of micelle encapsulated  $^{64}\text{Cu}$ -NOTA-UCNPs. At 1 hour after injection, UCNPs were observed inside of sinusoid, space of Disse, hepatocyte and Kupffer cells. Inside the hepatocytes, UCNPs were localized in cytoplasmic vesicles and some of the vesicles contained innumerable UCNPs (Fig. 17a-d). Also, UCNPs were found in bile canaliculi (Fig. 17e, f). At 24 hours after injection, interestingly, NPs were not found inside of hepatocyte, but remained in Kupffer cells (Fig. 17g, h). These findings suggest that injected UCNPs can be endocytosed by either hepatocytes or Kupffer cells in the liver and UCNPs which were endocytosed by hepatocytes were excreted via biliary excretion pathway. On the contrary, UCNPs which were endocytosed by Kupffer cells seemed to remain inside the cells until 24 hours after injection. Also, this TEM finding can explain remaining uptake in the liver at 24 hours after injection in *in vivo* PET image and *ex vivo* biodistribution results. A schematic figure of hepatobiliary excretion flow of micelle encapsulated  $^{64}\text{Cu}$ -NOTA-UCNPs was demonstrated in figure 17i. Micelle encapsulated  $^{64}\text{Cu}$ -NOTA-UCNPs flowed into hepatocytes dominantly and followed the hepatobiliary excretion.



i



**Cu-64-UCNP**



**Hepatocyte**

## Figure 17.

Observation of hepatobiliary excretion using TEM study. At 1 hour after injection of micelle encapsulated  $^{64}\text{Cu}$ -NOTA-UCNPs, **a**, UCNPs were observed inside of sinusoid. **b**, in the space of Disse. **c**, Multiple UCNPs were found in the intracellular space of Kupffer cell. **d**, UCNPs were found in cytoplasm of hepatocyte in vesicular structure. **e**, UCNPs were found inside bile canaliculi. **f**, UCNPs were visualized in the magnified image of bile canaliculi. At 1 hour after injection of micelle encapsulated UCNP, **g**, UCNP was not seen in hepatocyte, **h**, but seen in Kupffer cell at 24 hour images. Arrows indicated UCNPs. Asterisks indicated red blood cell. **i**, A schematic figure of hepatobiliary excretion flow of micelle encapsulated  $^{64}\text{Cu}$ -NOTA-UCNPs was represented. UCNPs were mixed in the sinusoid and penetrated sinusoidal endothelial cells dominantly. And UCNPs were endocytosed and exocytosed in hepatocytes. Partly, Kupffer cell engulfed UCNPs. Exocytosed UCNPs in hepatocytes flowed into bile canaliculi and bile ductile.

## Discussion

In this study, I demonstrated and quantified that micelle encapsulated  $^{64}\text{Cu}$ -NOTA-UCNPs had substantial hepatobiliary excretion in microPET, ULI and *ex vivo* method concordantly.  $^{64}\text{Cu}$ -NOTA labeling method was appropriate for 72 hours long time biodistribution. As in our *ex vivo* biodistribution results, over 80% clearance from initial liver uptake within 72 hours and over 40% of total injected dose excretion by feces within 24 hours after injection of NPs are quite substantial compared to previous reports which showed hepatobiliary excretion of NPs (26, 27, 44). In one study, intravenously injected  $^{64}\text{Cu}$  labeled nano shell was excreted via intestine after initial uptake in the liver, however, only 13% of injected dose was found in feces in 44 hours (44). Kumar et al. reported good hepatobiliary excretion property of silica NP but initial liver uptake was decreased to 50% at 120 hours after injection, which was slower than our result (27). Based on our result of over 80% clearance from initial liver uptake within 72 hours, we can estimate that there might be 4% residual micelle encapsulated  $^{64}\text{Cu}$ -NOTA-UCNPs after 6 days and 0.8% after 9 days of post-injection.

Hepatobiliary excretion is a complex mechanism. The hepatobiliary system consists of Kupffer cell, hepatocyte, bile duct and blood vessel. The particles by hepatobiliary excretion mostly do not undergo renal excretion. Generally NPs with size over 8 nm cannot be filtrated by glomeruli and thus cannot be excreted by kidney. Burn et al. reported that smaller sized NPs less than 6 nm were cleared out of the animal by renal excretion effectively (45). NPs with size

over 8 nm initially retained in liver or spleen after intravenous administration, because the organs have high perfusion rate and fenestrated endothelium (46). After the NPs have reached to liver, the NPs can be endocytosed by Kupffer cells or hepatocytes. Since hepatocytes are within the pathway of biliary excretion, the NPs endocytosed by hepatocytes will enhance hepatobiliary excretion (47). To be endocytosed by hepatocyte, NP should be less than 100 nm because size is a critical factor to fenestrate endothelium of liver (46). Also, size of 50 nm is optimal to maximize a rate of endocytosis in several types of NPs (48, 49).

Thus, the size of NP of the present study (34.1 nm) may be optimal for hepatobiliary excretion. The size of UCNPs is 31 nm (diameter) x 37 nm (length) and the size of micelle encapsulated <sup>64</sup>Cu-NOTA-UCNPs is about 34 nm. Our results showed an optimal size of NPs within 50 nm and it was rapidly excreted by gastrointestinal track. Kumar et al. mentioned that silica NPs with 20-25 nm were accumulated in liver and the excretion route was through feces via the hepatobiliary system (27). According to Brucer, small particles less than 100nm were phagocytosed to a large extent by Kupffer cells (50), on the other hand, entrapment in the space of Disse may play a significant role in the removal of larger colloids (10 to 1000 nm) (51). In this study, the amount of endocytosis by hepatocyte was higher than Kupffer cell. Therefore, I speculated that the space of Disse might be a dominant role as a pathway to hepatocytes.

The surface modification of UCNPs is a key mechanism to elevate the elimination of NPs (52). UCNPs have hydrophobic surfaces after core synthesis, therefore, hydrophilic phase is a prerequisite condition for *in vivo* or *in vitro* study.

Previous reports mentioned the immune and inflammatory process due to hydrophobicity of NPs and shape by gold NPs and carbon nanotubes (53). PEGylation decreases first pass extraction and increases NP serum half-life, which causes prolonged retention of NPs within liver parenchyma (54). PEG has found variable applications ranging from a preparation of cosmetics, pharmaceutical and medical production, and medical applications. PEG has many advantages for biological applications thanks to low toxicity, no immunogenicity and no metabolic degradation during clearance from the body. NPs coated with PEG form stable colloids in water and PEG reduces the non-specific binding of proteins or cell surfaces (55-57). Likewise, a new ultrasmall superparamagnetic iron oxide agent (new USPIO) with monodisperse iron oxide core and multiple-interaction ligands such as polyDOPA and PEG enhanced stability, which proved that high stability of new USPIO particle in various salt concentrations, pH levels, temperatures, and in a high iron concentration (58).

Micelle encapsulation method could facilitate faster hepatobiliary excretion. The encapsulation method of NPs has been developed by Dubertret *et al.* (28), Fan *et al.* (29), Wu *et al.* (31) and Lee *et al.* (32) since 2002. Recently, Lee *et al.* (32) achieved both multifunctionality and hydrophilicity of NPs as one-step method. Polysorbate 60 and NOTA-C<sub>18</sub> (32) could be labeled with <sup>64</sup>Cu easily. A branched polyethylene glycol (PEG) and a C<sub>18</sub> stearate tail were suitable for biocompatibility in UCNPs. There were several reports that showed hepatobiliary excretion of liposome (59) and micelles (60, 61). As I compare a different encapsulation method of UCNPs, polyacrylic acid-coated UCNPs (PAA-UCNPs)

with an average diameter of 11.5 nm and -10mV showed larger uptake in the spleen than liver after 24 hours. Significantly decreased uptake was observed at 14 days post-injection. Micelle encapsulated  $^{64}\text{Cu}$ -NOTA-UCNPs showed remarkable hepatobiliary excretion compared to PAA-UCNPs (62). Another study presented that PEG-silica NPs exhibited relatively longer blood circulation times and lower uptake by the reticuloendothelial system organs than OH-silica NPs and COOH-silica NPs (63). The surface modifications (-COOH, -OH or -NH<sub>2</sub> functional groups) were related with the impact of TiO<sub>2</sub> NPs, on the survival of a variety of cancer cell lines. In addition, by altering the surface chemistry of TiO<sub>2</sub> particles, the toxicity of TiO<sub>2</sub> could be modified. In general, NH<sub>2</sub>, and OH surface modified TiO<sub>2</sub> exhibited greater toxicity than COOH modified TiO<sub>2</sub>. TiO<sub>2</sub> toxicity was much more dependent on the surface chemistry of TiO<sub>2</sub> NPs (64, 65).

Different core particles are a significant factor of the rate of hepatobiliary excretion and aggregation. Quantum dots showed persistent retention over 100 days in variable organs and caused tissue toxicity (66). And previous work indicated that CdSe QDs were highly toxic to cells under UV illumination for extended periods of time, but little is known about the mechanism of metabolism or clearance of QD probes injected into living animals (67). PEGylated  $^{198}\text{Au}$  (31 nm, -10.1 mV) showed hepatobiliary accumulation from 1 hour to 24 hours post-injection contrary to our results of fast hepatobiliary excretion of micelle encapsulated  $^{64}\text{Cu}$ -NOTA-UCNPs. And PEGylated  $^{198}\text{Au}$  and mesoporous SiO<sub>2</sub> showed aggregation in lung, because the hydrophilicity can affect the aggregation of NPs via intravenous injection causing pulmonary embolism by blocking the

capillaries (52, 68). However, our PET images, *ex vivo* study and TEM revealed no evidence of aggregation of micelle encapsulated  $^{64}\text{Cu}$ -NOTA-UCNPs. Early blood flow in lungs showed increased uptake at 0.25 hour PET image, but further delayed images after 1 hour showed no uptake in lung. It revealed wash-out pattern clearly (Fig. 6). Also *ex vivo* biodistribution study revealed remarkably decreased activity serial follow-up in lung (Fig. 8). Moreover, TEM images of liver after 1 hour and 24 hours post-injection showed scattered UCNPs. Therefore, I clearly demonstrated no aggregation in blood circulation after micelle encapsulated  $^{64}\text{Cu}$ -NOTA-UCNPs injection. This finding can be due to the property of a core particle. *In vivo* study of micelle encapsulated  $^{64}\text{Cu}$ -NOTA-UCNPs demonstrated better hepatic excretion than other core particles. *In vivo* biodistribution studies of the 55 nm  $^{64}\text{Cu}$ -DOTA-PEG-Au nanocages showed faster hepatobiliary excretion than previous Au NPs. However, the hepatic excretion was markedly lower than our results; 60 % ID/g at 1 hour post-injection and  $41.6 \pm 1.5$  % ID/g at 24 hours in  $^{64}\text{Cu}$ -DOTA-PEG-Au nanocages vs.  $45.04 \pm 2.13$  % ID/g at 1 hour and  $13.16 \pm 0.62$  % ID/g at 24 hours in micelle encapsulated  $^{64}\text{Cu}$ -NOTA-UCNPs (69). Moreover, the effect of PEGylation of NPs in *in vivo* study has not been evaluated well (70). Meanwhile, PEGylation can move target tumors through the well-known enhanced permeability and retention (EPR) effect because it reduces nonspecific accumulation and prolonged blood circulation of inorganic NPs owing to their large hydrodynamic diameters, which are above the renal filtration threshold (71, 72). Additional functional moiety with PEGylation can be applicable for variable clinical purposes.

In this study, micelle encapsulation method in UCNPs improved image

quality of *in vivo* PET, ULI and TEM. First, there was no aggregation of micelle encapsulated  $^{64}\text{Cu}$ -NOTA-UCNPs in *in vivo* PET and ULI. The aggregation of NPs in lung is one of the most significant side effects, because aggregated NPs cause pulmonary embolism and death. But, this study demonstrated early washout pattern of micelle encapsulated  $^{64}\text{Cu}$ -NOTA-UCNPs in lung and heart. And *in vivo* PET, ULI and *ex vivo* method showed no aggregation of UCNPs concordantly. NPs in biological fluids are covered by a biomolecular corona. Several NPs of very different materials and size are trafficked to the lysosomes without export and degradation. This means that the corona screens the properties of the bare material and is retained until degradation in the lysosomes, like a general Trojan-horse paradigm (73). Micelle encapsulation method masked the bare UCNP as the corona protein UCNPs. Therefore, micelle encapsulated  $^{64}\text{Cu}$ -NOTA-UCNPs might show the characteristics of good dispersibility and decrease phagocytosis by Kupffer cells. Hydrophobic UCNPs were capped by oleic acid. They are dispersible evenly in nonpolar organic solvents and not in an aqueous solution or biological buffer. UCNPs capped by oleic acid show high and long standing stability more than several years in hydrophobic solvent. However, hydrophobicity limits their applications for *in vivo* and *in vitro* study, where hydrophilicity is a prerequisite. Ligand exchange is the most popular method to modify the surface of UCNPs by replacing the original hydrophobic ligands with some hydrophilic ligands without the obvious influence on the chemical and optical properties of UCNPs. The hydrophobic oleic acid ligand with a long-chain hydrocarbon and a carboxyl group ( $-\text{COOH}$ ) coordinates with the lanthanide ions (Yttrium) on the nanoparticle

surface. A large variety of ligands have been reported, including poly (acrylic acid) (PAA), PEG-phosphate, mercaptopropionic acid (MPA), hexanedioic acid (HDA), 3-dimercaptosuccinic acid (DMSA), mercaptosuccinic acid (MSA), citrate, 1,10-decanedicarboxylic (DDA), mercaptonodecanoic acid (MUA), and poly-(amidoamine) (PAMAM), which can be added to carry variable functional groups (74). Previous report demonstrated that UCNP coated by PEG-phospholipids has intact luminescence under acidic and neutral conditions, and good dispersibility. Moreover, endocytosis and exocytosis of UCNPs mediated by dyneins and kinesins in cellular level were confirmed by additional studies employing inhibitors and spectroscopic measurements. Interestingly, the movement of single UCNP without aggregation has been observed in HeLa cell under the real time live cell technique (34). Also, on the TEM image, I could observe multiple UCNPs without aggregation in sinusoid, hepatocyte, Kupffer cell and bile canaliculi. Moreover, UCNPs showed good dispersibility as a single particle in the collected feces and urine. Therefore, the characteristics of good dispersibility in UCNPs with corona protein improved the image quality and affected fast hepatobiliary excretion.

The surface charges may be one of the significant factors controlling hepatobiliary excretion. The surface charges of UCNPs and micelle encapsulated <sup>64</sup>Cu-NOTA-UCNPs were -27.1 mV and -6.63 mV, respectively. It has been reported that NPs with neutral or zwitterionic charge had a tendency to decrease of plasma adsorption. Cationic particles are more cytotoxic and likely to induce hemolysis and platelet aggregation than neutral or anionic particle (62). In this study, phagocytosis of UCNPs might be reduced owing to the characteristics of

anion near neutral charge of micelle encapsulated  $^{64}\text{Cu}$ -NOTA-UCNPs and UCNPs (75). The anionic NPs may be endocytosed through the interaction with the positive site of the proteins in membrane, and can be highly captured by cells because of their repulsive interactions with the negatively charged cell surface (76). However, Souris et al. reported contrarily that mesoporous silica NPs with highly charged moieties (+34.4 mV at pH 7.4) were quickly excreted than those with less charged moieties (-17.6 mV at pH 7.4). However, they only compared NPs with surface charge of 34.4 and -17.6 mV (26). Meanwhile, the positively charged UCNP-polyethylenimine (PEI) showed higher cellular uptake in comparison with its neutral or negative counterparts (77). It could be due to PEI or charge effect. The multiple comparisons of NPs with various surface charges are warranted to conclude which is more suitable surface charge for hepatobiliary excretion.

The geometry of NPs can affect rapid excretion. For example, gold NPs have high toxicity, irreversible binding to the DNA, extremely low excretion and bio-inert. But nanoclustering design of gold NPs elevated the excretion rate of gold NPs, although remaining gold NPs were observed more than several weeks (78). Nonporous  $\text{SiO}_2$  and their amine-modified counterparts exhibited high liver affinity in liver and spleen than other porous  $\text{SiO}_2$  but amine-modified mesoporous nanorods showed higher lung affinity (52). Meanwhile, a surface angle of NPs is related with phagocytosis. As the angle is defined as between the membrane normal at the point of attachment and the line defining the particle curvature at this point, particles less than  $45^\circ$  are internalized successfully (79, 80).

The physicochemical properties are associated with biliary excretion. Specificity of hepatocyte uptake for various compounds in nuclear medicine field is due to carrier-mediated mechanisms and membrane-bound transport proteins. Independent mechanisms of hepatocyte uptake across the sinusoid membrane have been described for several classes of compounds: anions, cations, neutral compounds, and bile salts (81). Excretion into bile involves an active transport process. The intrahepatic membrane high bile-to-plasma concentration gradients is a principle of hepatobiliary imaging agents (82). From this point, the elimination process is relatively passive essentially following the flow of bile through biliary tree. Progression of the compound is influenced primarily by the tone of the sphincter of Oddi and the patency of the bile ducts.  $^{99m}\text{Tc}$ -N-substituted iminodiacetic acid (IDA) compounds, for hepatobiliary scan is facilitated by carrier-mediated, non-sodium-dependent, organic anionic pathways similar to those responsible for bilirubin uptake. On entering a hepatocyte, various substances may interact with cytoplasmic proteins such as ligandin, which has glutathione transferase activity be metabolized through the action of the smooth endoplasmic reticulum or be excreted unchanged, as is the case of  $^{99m}\text{Tc}$ -IDA compounds (51). Therefore, I consider the low passive membrane permeability and organic anion transporting polypeptide (OATP) as a candidate transporter of micelle encapsulated  $^{64}\text{Cu}$ -NOTA-UCNPs. OATP transporters expressed on the hepatic sinusoid membrane and were related with biliary excretion (83). Meanwhile, breast cancer resistance protein (Bcrp, rodents; BCRP/*ABCG2*, human) played a significant role in the efflux activity in liver and kidney (84). Other canalicular efflux transporters

[P-glycoprotein (P-gp), multidrug resistance-associated protein 2 (Mrp2, rodents; MRP2, humans)] are important for the hepatic excretion. However, relatively large size of UCNPs might be hard to be transported by these transporting systems. Further study is needed.

A concern of degradation of the surface materials on NPs has been mentioned in the polymer shell recently (85). The thiol layer confers the significant benefit of making the particles stable and isolable and allowing them to be re-suspended if desired (86). However, a recent study reported that a partial separation of the organic shell from the inorganic core was caused by proteolytic enzymes present in the cellular compartments. And *in vivo* degradation of the polymer shell was due to similar proteolytic digestion (87). Although the coordination complex of gold NPs and thiol group was strong, a partial degradation was observed. Likewise, the surface of UCNP and carboxylate (COO<sup>-</sup>) of oleic acid has strong coordination complex and the coordination complex between the double bond of carboxylate (COO<sup>-</sup>) and the surface of UCNPs might not be weaker than that of gold NPs and thiol group. But hydrophobic van der Waals interaction between oleic acid and alkyl-PEG or NOTA-C<sub>18</sub> might have weak coherence. Therefore, comparison PET study of free <sup>64</sup>Cu, <sup>64</sup>Cu-NOTA-C<sub>18</sub> and micelle encapsulated <sup>64</sup>Cu-NOTA-UCNPs was done. In case of detachment of free <sup>64</sup>Cu, persistent liver uptake on PET should be visualized until 24 hours. However, I could not observe severe retentional uptake of liver on PET after 24 hour post-injection of micelle encapsulated <sup>64</sup>Cu-NOTA UCNPs. Moreover, PET image of <sup>64</sup>Cu-NOTA-C<sub>18</sub> showed large amount of renal excretion in early time points and hepatic excretion as further delayed images.

However, on PET of micelle encapsulated  $^{64}\text{Cu}$ -NOTA UCNPs, I observed minimal renal excretion about 1% and most excretion was done by intestine and feces. It was markedly different from free  $^{64}\text{Cu}$  and  $^{64}\text{Cu}$ -NOTA- $\text{C}_{18}$ . Additionally, collected fecal materials and urine revealed intact UCNP signals. And concordant results with PET and *ex vivo* method revealed intact micelle encapsulated  $^{64}\text{Cu}$ -NOTA UCNPs. Moreover, liver TEM images showed intact UCNPs with good dispersibility in hepatobiliary pathway. I confirmed that the amount of detachment might be negligible due to a different excretion pathway of NPs.

To confirm the detachment of radiolabeling from UCNP, further studies should be evaluated. Kreyling et al. (87) synthesized monodisperse radioactively labeled gold nanoparticles ( $^{198}\text{Au}$ ) and engineered an  $^{111}\text{In}$ -labelled polymer shell around them. Upon intravenous injection into rats, quantitative biodistribution analyses revealed that  $^{198}\text{Au}$  accumulated mostly in liver and part of the  $^{111}\text{In}$  showed a non-particulate biodistribution similar to intravenous injection of chelated  $^{111}\text{In}$ . Further *in vitro* studies showed that degradation of the polymer shell was caused by proteolytic enzymes in liver. The results demonstrated that NPs with high colloidal stability can change their physicochemical properties *in vivo*. Likewise, I can design dual radiolabeling technique in the core and capping of UCNP. Samarium-153-labeled ( $^{153}\text{Sm}$ ) ethylenediamine tetramethylenephosphonic acid (EDTMP)-UCNP is a bimodal imaging agent.  $^{153}\text{Sm}$  emits beta particles and gamma rays. Therefore, both single-photon emission computed tomography (SPECT) and ULI can be obtained by  $^{153}\text{Sm}$ -EDTMP-UCNP (88). Although an experiment of dual radiotracers in UCNP has not been performed,  $^{64}\text{Cu}$  (PET,

$T_{1/2}$ =12.7 hours),  $^{67}\text{Ga}$  (SPECT,  $T_{1/2}$ =3.26 days),  $^{111}\text{In}$  (SPECT,  $T_{1/2}$ =2.8 days) and  $^{89}\text{Zr}$  (PET,  $T_{1/2}$ =3.3 days) might be a potential capping radiopharmaceutics of  $\text{NaLuF}_4:\text{Yb,Tm},^{153}\text{Sm}$ . This dual tracer experiment might reveal the degree of detachment of capping material from UCNPs in *in vivo*. The biodistribution study of *in vivo* PET and/or SPECT can reveal the difference of core and shell of UCNP, therefore, the stability of radiolabeling on UCNP can be estimated. Moreover, *in vitro* study can elucidate the effect of proteolytic enzymes in Kupffer cells and other cell lines. Further study is recommended.

Phagocytosis was originally discovered in macrophages. Pinocytosis is present in all types of cells in four forms, such as clathrin-dependent endocytosis, caveolae-dependent endocytosis, macropinocytosis, and clathrin-and caveolae-independent endocytosis (89-91). The size of vesicle involved in clathrin-coated pit is about 100~200 nm, while the size involved in caveolae-mediated endocytosis is about 60-80 nm. Particles as large as 500 nm were internalized by cells via energy-dependent process (92, 93). Meanwhile, the clathrin-endocytic mechanism of the cationic UCNP-PEI was revealed by colocalization, chemical, and genetic inhibitor studies (77). Except for caveolae-mediated endocytosis, all the other pathways have a relationship with lysosomes. In the process of caveolae-mediated endocytosis, the NPs do not fuse with lysosomes after their entry into cells. After engulfed in the cells, the vesicles containing NPs fuse with caveosomes or multivesicular body which have a neutral pH (94) and can be delivered to endoplasmic reticulum or Golgi complex, or even released to outside the cells (95). Surface coatings on UCNPs would play an important role in their cellular entry

through the plasma membrane and the corresponding internalization pathways (96, 97).

For this reason, I thought that caveolae-mediated endocytosis will be beneficial for enhancement of concentration of targeting position and improvement of therapeutic effect. There are three isoforms of caveolin in mammalian cells. Caveolin-1 and -2 are abundant in most non-muscle cells (such as endothelial cells, fibroblasts and adipocytes), caveolin-3 is muscle specific, and absent in neurons and leukocytes (92). By binding to the receptors on the plasma membrane, NPs or pathogens, like simian virus 40 and cholera toxin, can interact with the receptors to induce the formation of the flask-shaped vesicles, which are cut off from the membrane by dynamin. Similar to clathrin-dependent endocytosis, caveolar vesicles require actin to move and intact microtubules to traffic within the cell. It has been reported that UCNPs encapsulated by PEG-phospholipids were internalized through endocytosis, transported by microtubule-dependent motor proteins (dyneins), accumulated at the perinuclear region, transported by another type of motor proteins (kinesins), and finally released out of the cells through exocytosis (34)

Exocytosis of micelle encapsulated  $^{64}\text{Cu}$ -NOTA UCNPs in hepatocyte was observed in this study. However, the mechanisms of exocytosis and cell signaling pathways are yet elusive. There are multiple factors affecting the exocytosis of NPs. First, the size of NP is related with the extent of excretion. Smaller NPs were more easily released from HepG2 cells. The same trend was observed for transferrin-coated gold NPs (98). One explanation for this observation could be the existence

of ligands on the surface of the NPs that interact with specific receptors affecting release. Another possibility for the effect of NP size on the exocytosis rate was proposed by Panyam et al. (99, 100). Based on their proposed recycling process, the cell has at least two possible intracellular compartments (endosomes and lysosomes/cytoplasm). Following endocytosis, a fraction of the NPs are delivered to the lysosomes or translocates from the recycling endosomes into the cytoplasm. Other NPs remain in the endosomes or are recycled back to the surface of the cell. The size of different NPs could affect their delivery into the fast or slow recycling compartments (101). Fang et al. found that exocytosis of fluorescent nanodiamonds is significantly slower than exocytosis of D-penicillamine coated CdSe/ZnS QDs from HeLa cells (102, 103). They proposed that this difference was the combined effect of the larger particle size and the aggregation of the fluorescent nanodiamond particles in slow turn over compartments. Jin et al. studied the size dependence of single-walled carbon nanotubes (SWNTs) exocytosis using single particle tracking techniques. The exocytosis rates of SWNTs in NIH-3T3 cells followed the same trend as above: smaller SWNTs can be exocytosed faster than larger SWNTs (104). Both theoretical and experimental studies of endocytosis confirmed that there is an optimal NP size (40–60nm) for efficient entry into cells, which can also be affected by several other factors such as membrane-NPs binding energy, protein or ligand density on the surface of NPs, and NP curvature (105-109). Second, NP shape is also important for both endocytosis and exocytosis processes (105, 110-112). In the case of exocytosis, the fraction of rod-shaped NPs released from HeLa and SNB 19 cell lines was much higher than spherical-shaped NPs. However, the release of NPs

from STO cells was the same for both rod- and spherical-shaped NPs. The observed differences between various cell lines were related to the cell type effect (the exocytosis pathways might be different in various cells) (113). Third, different surface modifications have decisive effects on the exocytosis profile of NPs. Yanes et al., investigated the effect of different surface modification of MSNs (phosphonate, folate, and polyethylenimine (PEI)) on the release of NPs from A549 cells. After 6 h, 84%, 66%, and 49% of the phosphonate-MSNs, folate-MSNs and PEI-MSNs had been released, respectively (114). Fourth, vesicle known as early endosomes is a significant factor of exocytosis. The newly formed vesicles mature into late endosomes or multivesicular bodies, and then into lysosomes, which have an acidic pH. When these vesicles contained NPs, they were transported along microtubules from the periphery to the perinuclear region by dynein motors (34, 102, 115). These internalized NPs could then be actively transported to the periphery and exocytosed by cells, or fused with lysosomes and other cytoplasmic compartments that have a slow turnover (99, 100). For example, Wang et al. measured the intracellular uptake and excretion of CuO NPs in A549 cells and found that a portion of NPs, which were located in mitochondria and nucleus, could not be excreted by the cells (116). Similarly, based on findings by Chu et al., clusters of silica NPs in lysosomes are more easily exocytosed by H1299 cells compared to single NP in the cytoplasm (117). In a typical exocytosis process, the NPs are initially trapped in lysosomes before their transportation to the cell membrane for excretion. Stayton et al. showed that NPs that left the endocytotic vesicles or lysosomes and translocated into the cytoplasm had greater difficulty in

exocytosis (118). Moreover, NPs that are trapped in the slow turn-over compartments such as lysosomes, need a larger number of proteins and receptors for their exocytosis. Since exocytosis is an active process, metabolic inhibitors can inhibit exocytosis of NPs. Panyam and coworkers (99) showed that the use of metabolic inhibitors of sodium azide and deoxyglucose could reduce the exocytosis of poly (D,L-lactide-co-glycolide) NPs by 40%. Fifth, translocation of NPs across vital barriers should be observed. In another study, charge effects on the transcytosis of poly (ethylene glycol)-D,L-poly lactide (PEG-PLA) NPs by epithelial canine kidney MDCK cells were investigated (119). The results showed that both cationic and anionic NPs were delivered to the basolateral site. However, only a small fraction of anionic NPs were co-localized in degradative lysosomes. Hence, NP surface charge not only impacts uptake efficiency, but also can influence intracellular trafficking (120, 121). Due to a variety of cell types, biological environments, and types of NPs, there are still many indistinct pathways that can result in exocytosis. A better understanding of exocytosis and related cellular functions and their dynamics will shed more light on the design of NPs in-demand for different medical applications.

Our present study, UCNPs presented the excellent hepatobiliary excretion and fecal material had intact characteristics of UCNPs. There was no evidence of biodegrade after the excretion of hepatobiliary and urinary system. Using TEM image, I demonstrated several NPs in MPS after 24 hour post-injection. I now know that small amount of micelle encapsulated  $^{64}\text{Cu}$ -NOTA-UNCNPs was excreted via urine which was verified by both the radioactivity and luminescence but the

amount was too small to be visualized in *in vivo* PET imaging. There were several reports showing urinary excretion of NPs with larger size than the pore of the glomerulus. However, the mechanism is not clearly evaluated (63). And an interesting report of renal clearance of silica NPs with a size of over 50 nm was reported, which is much larger than the kidney filtration threshold. Our results showed the small amount of renal excretion with a 34.4 nm NP.

Micelle encapsulated  $^{64}\text{Cu}$ -NOTA labeling method using microPET was safe and efficient. Mice after intravenous injection of micelle encapsulated  $^{64}\text{Cu}$ -NOTA-UCNPs (12  $\mu\text{g}$  / mouse) had no side effect. However, the 13 times dose escalation compared with PET was needed to obtain the signal of ULI (158  $\mu\text{g}$  / mouse). When I injected UCNPs via tail vein for ULI, mice showed no significant side effect till 24 hours. However, the region of interest for obtaining ULI was transmitted by repeated NIR 980 nm laser power (21 W (30 A),  $\sim 300 \text{ mW}/\text{cm}^2$ , EMCCD Gain = 250, exposure time = 10 s), which caused death due to hepatic fibrosis and congestion of inferior vena cava. Therefore, I could not obtain serial optical image in an individual mouse inevitably. There was no evidence of toxicity of UCNPs, but fibrosis due to laser effect caused death. Moreover, the acquisition of ULI was difficult due to the limited penetration depth. Although BALB/c nude mice have transparent skin without hair, the intensity of visible light after NIR excitation was remarkably reduced due to skin, peritoneum or thorax, and so on. Therefore, *ex vivo* images showed higher signal intensity than *in vivo* or *in situ* ULI. Meanwhile, this limitation of penetration depth elucidates the photodynamic therapy of skin cancer (122). As the intrinsic characteristics of UCNPs are

available for optical, PET, SPECT/CT and MRI, researchers can use UCNPs for better imaging and therapy material. Here, I demonstrated the advantage of UCNPs as promising NPs for *in vivo* PET and ULI.

In this study, I observed the physiologic pathway of micelle encapsulated  $^{64}\text{Cu}$ -NOTA-UCNPs by endocytosis and exocytosis in hepatocytes. Micelle encapsulated  $^{64}\text{Cu}$ -NOTA-UCNPs via the venous flow have a confluence in sinusoid and infiltrate intracellular space. The micelle encapsulated  $^{64}\text{Cu}$ -NOTA-UCNPs were excreted by biliary canaliculi and expelled in feces. The findings were confirmed by TEM images. At 1 hour TEM images, UCNPs were well observed in sinusoid, space of Disse, hepatocyte, bile canaliculi and Kupffer cell. However, UCNPs were located only in Kupffer cell at 24 hour TEM images. And the hepatobiliary excretion of micelle encapsulated  $^{64}\text{Cu}$ -NOTA-UCNPs were observed from gall bladder to duodenum, ileum, jejunum and whole large bowel in ULI, PET and *ex vivo* method concordantly.

There are several limitations. First, I have no significant side effect of micelle encapsulated  $^{64}\text{Cu}$ -NOTA-UCNPs in this study excluding laser effect. However, I did not analyze blood chemistry or hematology of mice. Additional long-term study of toxicity is recommended. Second, incidental death of mice was inevitable although I tried to obtain serial image of *in vivo* ULI. The technique of high energy of laser and long exposure time should be modified by the development of EMCCD. Third, our *in vivo* biodistribution study demonstrated hepatobiliary excretion during 72 hours. Relatively long half-life, 762 minutes of  $^{64}\text{Cu}$  revealed more than 80% hepatic clearance at 72 hours post-injection.

However,  $^{89}\text{Zr}$  with a half-life of 78.4 hours might be more suitable than  $^{64}\text{Cu}$  in this case (123). Fourth, I observed over 80% clearance from initial liver uptake within 72 hours and it might be considered as a safe material. However, further study using variable drugs affecting hepatic metabolism is recommended to enhance an elimination of remaining UCNPs in Kupffer cells. Fifth, possibility of detachment of free  $^{64}\text{Cu}$  or  $^{64}\text{Cu-NOTA-C}_{18}$  from micelle encapsulated  $^{64}\text{Cu-NOTA-UCNPs}$  cannot be excluded. Therefore, dual radiotracer labeling method of UCNP can be considered to quantify the amount of the detachment.

## Conclusion

In conclusion, I demonstrated the feasibility of bimodal *in vivo* imaging characteristics of micelle encapsulated  $^{64}\text{Cu}$ -NOTA-UCNP and showed the substantial hepatobiliary excretion through *in vivo* microPET, ULI, and *ex vivo* biodistribution study. This bimodal imaging characteristic is ideal for evaluation of excretion pattern of NP, because PET imaging is suitable for accurate quantification of biodistribution and ULI can be used for confirmation of UCNP. Moreover, by well characterization of imaging property and excretion pattern of micelle encapsulated  $^{64}\text{Cu}$ -NOTA-UCNPs, the NPs could be used for bimodal ULI and PET imaging agent for a variety of purposes by adding further functional moiety.

## References

1. Seo J, Ren G, Liu H, Miao Z, Park M, Wang Y, et al. In Vivo Biodistribution and Small Animal PET of <sup>64</sup>Cu-Labeled Antimicrobial Peptoids. *Bioconjugate chemistry*. 2012;23(5):1069-79.
2. Kang JS, Yum YN, Park SN. Cytotoxicity and DNA Damage Induced by Magnetic Nanoparticle Silica in L5178Y Cell. *Biomol Ther*. 2011;19(2):261-6.
3. Abdelhalim MA, Jarrar BM. Histological alterations in the liver of rats induced by different gold nanoparticle sizes, doses and exposure duration. *Journal of nanobiotechnology*. 2012;10:5.
4. Grosse S, Evje L, Syversen T. Silver nanoparticle-induced cytotoxicity in rat brain endothelial cell culture. *Toxicol in Vitro*. 2013;27(1):305-13.
5. Manke A, Wang L, Rojanasakul Y. Mechanisms of nanoparticle-induced oxidative stress and toxicity. *BioMed research international*. 2013;2013:942916.
6. Bottrill M, Green M. Some aspects of quantum dot toxicity. *Chem Commun (Camb)*. 2011;47(25):7039-50.
7. Nguyen KC, Rippstein P, Tayabali AF, Willmore WG. Mitochondrial Toxicity of Cadmium Telluride Quantum Dot Nanoparticles in Mammalian Hepatocytes. *Toxicol Sci*. 2015.
8. YF Salykina, VV Zherdeva. Biodistribution and clearance of quantum dots in small animals *Proc SPIE* 2011;Volume 7999
9. East BW, Boddy K, Williams ED, Macintyre D, McLay AL. Silver

retention, total body silver and tissue silver concentrations in argyria associated with exposure to an anti-smoking remedy containing silver acetate. *Clin Exp Dermatol.* 1980;5(3):305-11.

10. Matuk Y, Ghosh M, McCulloch C. Distribution of silver in the eyes and plasma proteins of the albino rat. *Can J Ophthalmol.* 1981;16(3):145-50.

11. Van der Zande M, Vandebriel RJ, Van Doren E, Kramer E, Herrera Rivera Z, Serrano-Rojero CS, et al. Distribution, elimination, and toxicity of silver nanoparticles and silver ions in rats after 28-day oral exposure. *ACS Nano.* 2012;6(8):7427-42.

12. Hadrup N, Lam HR. Oral toxicity of silver ions, silver nanoparticles and colloidal silver--a review. *Regul Toxicol Pharmacol.* 2014;68(1):1-7.

13. Zhu X, Chang Y, Chen Y. Toxicity and bioaccumulation of TiO<sub>2</sub> nanoparticle aggregates in *Daphnia magna*. *Chemosphere.* 2010;78(3):209-15.

14. Wang JX, Chen CY, Liu Y, Jiao F, Li W, Lao F, et al. Potential neurological lesion after nasal instillation of TiO<sub>2</sub> nanoparticles in the anatase and rutile crystal phases. *Toxicol Lett.* 2008;183(1-3):72-80.

15. Chen HW, Su SF, Chien CT, Lin WH, Yu SL, Chou CC, et al. Titanium dioxide nanoparticles induce emphysema-like lung injury in mice. *FASEB J.* 2006;20(13):2393.

16. Xie G, Wang C, Sun J, Zhong G. Tissue distribution and excretion of intravenously administered titanium dioxide nanoparticles. *Toxicol Lett.* 2011;205(1):55-61.

17. Zhang XD, Wu HY, Wu D, Wang YY, Chang JH, Zhai ZB, et al.

- Toxicologic effects of gold nanoparticles in vivo by different administration routes. *Int J Nanomedicine*. 2010;5:771-81.
18. De Jong WH, Hagens WI, Krystek P, Burger MC, Sips AJ, Geertsma RE. Particle size-dependent organ distribution of gold nanoparticles after intravenous administration. *Biomaterials*. 2008;29(12):1912-9.
19. Semmler-Behnke M, Kreyling WG, Lipka J, Fertsch S, Wenk A, Takenaka S, et al. Biodistribution of 1.4- and 18-nm gold particles in rats. *Small*. 2008;4(12):2108-11.
20. Lankoff A, Arabski M, Wegierek-Ciuk A, Kruszewski M, Lisowska H, Banasik-Nowak A, et al. Effect of surface modification of silica nanoparticles on toxicity and cellular uptake by human peripheral blood lymphocytes in vitro. *Nanotoxicology*. 2013;7(3):235-50.
21. Yu Y, Li Y, Wang W, Jin M, Du Z, Li Y, et al. Acute toxicity of amorphous silica nanoparticles in intravenously exposed ICR mice. *PLoS One*. 2013;8(4):e61346.
22. Gerashchenko BI, Gun'ko VM, Gerashchenko, II, Mironyuk IF, Leboda R, Hosoya H. Probing the silica surfaces by red blood cells. *Cytometry*. 2002;49(2):56-61.
23. Luo D, Saltzman WM. Nonviral gene delivery - Thinking of silica. *Gene Ther*. 2006;13(7):585-6.
24. Lu CW, Hung Y, Hsiao JK, Yao M, Chung TH, Lin YS, et al. Bifunctional magnetic silica nanoparticles for highly efficient human stem cell labeling. *Nano Lett*. 2007;7(1):149-54.

25. Kommareddy S, Amiji M. Biodistribution and pharmacokinetic analysis of long-circulating thiolated gelatin nanoparticles following systemic administration in breast cancer-bearing mice. *Journal of pharmaceutical sciences*. 2007;96(2):397-407.
26. Souris JS, Lee CH, Cheng SH, Chen CT, Yang CS, Ho JAA, et al. Surface charge-mediated rapid hepatobiliary excretion of mesoporous silica nanoparticles. *Biomaterials*. 2010;31(21):5564-74.
27. Kumar R, Roy I, Ohulchanskyy TY, Vathy LA, Bergey EJ, Sajjad M, et al. In Vivo Biodistribution and Clearance Studies Using Multimodal Organically Modified Silica Nanoparticles. *Acs Nano*. 2010;4(2):699-708.
28. Dubertret B, Skourides P, Norris DJ, Noireaux V, Brivanlou AH, Libchaber A. In vivo imaging of quantum dots encapsulated in phospholipid micelles. *Science*. 2002;298(5599):1759-62.
29. Fan HY, Yang K, Boye DM, Sigmon T, Malloy KJ, Xu HF, et al. Self-assembly of ordered, robust, three-dimensional gold nanocrystal/silica arrays. *Science*. 2004;304(5670):567-71.
30. Carion O, Mahler B, Pons T, Dubertret B. Synthesis, encapsulation, purification and coupling of single quantum dots in phospholipid micelles for their use in cellular and in vivo imaging. *Nat Protoc*. 2007;2(10):2383-90.
31. Wu H, Zhu H, Zhuang J, Yang S, Liu C, Cao YC. Water-soluble nanocrystals through dual-interaction ligands. *Angew Chem Int Edit*. 2008;47(20):3730-4.
32. Lee YK, Jeong JM, Hoigebazar L, Yang BY, Lee YS, Lee BC, et al.

Nanoparticles Modified by Encapsulation of Ligands with a Long Alkyl Chain to Affect Multispecific and Multimodal Imaging. *J Nucl Med.* 2012;53(9):1462-70.

33. Cheng L, Yang K, Zhang S, Shao M, Lee S, Liu Z. Highly-sensitive multiplexed in vivo imaging using pegylated upconversion nanoparticles. *Nano Res.* 2010;3(10):722-32.

34. Bae YM, Park YI, Nam SH, Kim JH, Lee K, Kim HM, et al. Endocytosis, intracellular transport, and exocytosis of lanthanide-doped upconverting nanoparticles in single living cells. *Biomaterials.* 2012;33(35):9080-6.

35. Abdul Jalil R, Zhang Y. Biocompatibility of silica coated NaYF<sub>4</sub> upconversion fluorescent nanocrystals. *Biomaterials.* 2008;29(30):4122-8.

36. Hilderbrand SA, Shao F, Salthouse C, Mahmood U, Weissleder R. Upconverting luminescent nanomaterials: application to in vivo bioimaging. *Chemical communications.* 2009(28):4188-90.

37. Lim SF, Riehn R, Tung CK, Ryu WS, Zhuo R, Dalland J, et al. Upconverting nanophosphors for bioimaging. *Nanotechnology.* 2009;20(40):405701.

38. Xiong L, Yang T, Yang Y, Xu C, Li F. Long-term in vivo biodistribution imaging and toxicity of polyacrylic acid-coated upconversion nanophosphors. *Biomaterials.* 2010;31(27):7078-85.

39. Kushihara H. Imaging in the study of membrane transporters. *Clinical pharmacology and therapeutics.* 2013;94(1):33-6.

40. Levin CS. New imaging technologies to enhance the molecular sensitivity of positron emission tomography. *P Ieee.* 2008;96(3):439-67.

41. Cao T, Yang Y, Gao Y, Zhou J, Li Z, Li F. High-quality water-soluble and surface-functionalized upconversion nanocrystals as luminescent probes for bioimaging. *Biomaterials*. 2011;32(11):2959-68.
42. Li Z, Zhang Y. An efficient and user-friendly method for the synthesis of hexagonal-phase NaYF<sub>4</sub>:Yb, Er/Tm nanocrystals with controllable shape and upconversion fluorescence. *Nanotechnology*. 2008;19(34):345606.
43. Park J, An K, Hwang Y, Park JG, Noh HJ, Kim JY, et al. Ultra-large-scale syntheses of monodisperse nanocrystals. *Nat Mater*. 2004;3(12):891-5.
44. Xie H, Wang ZJ, Bao A, Goins B, Phillips WT. In vivo PET imaging and biodistribution of radiolabeled gold nanoshells in rats with tumor xenografts. *International journal of pharmaceutics*. 2010;395(1-2):324-30.
45. Burns AA, Vider J, Ow H, Herz E, Penate-Medina O, Baumgart M, et al. Fluorescent Silica Nanoparticles with Efficient Urinary Excretion for Nanomedicine. *Nano Letters*. 2008;9(1):442-8.
46. Garnett MC, Kallinteri P. Nanomedicines and nanotoxicology: some physiological principles. *Occupational medicine*. 2006;56(5):307-11.
47. Longmire M, Choyke PL, Kobayashi H. Clearance properties of nano-sized particles and molecules as imaging agents: considerations and caveats. *Nanomedicine*. 2008;3(5):703-17.
48. Albanese A, Tang PS, Chan WC. The effect of nanoparticle size, shape, and surface chemistry on biological systems. *Annual review of biomedical engineering*. 2012;14:1-16.
49. Jani P, Halbert GW, Langridge J, Florence AT. The Uptake and

Translocation of Latex Nanospheres and Microspheres after Oral-Administration to Rats. *J Pharm Pharmacol.* 1989;41(12):809.

50. M B. Krieger, Liver scans, clearances, and perfusions. 1977.

51. Robert E. Henkin DB, Stephen M. Karesh, Gary L. Dillehay, Robert H. Wagner, James R. Halama, A. Michael Zimmer. *Nuclear Medicine* 2nd edition. Mosby. 2006.

52. Yu T, Hubbard D, Ray A, Ghandehari H. In vivo biodistribution and pharmacokinetics of silica nanoparticles as a function of geometry, porosity and surface characteristics. *J Control Release.* 2012;163(1):46-54.

53. Nam J, Won N, Bang J, Jin H, Park J, Jung S, et al. Surface engineering of inorganic nanoparticles for imaging and therapy. *Adv Drug Deliver Rev.* 2013;65(5):622-48.

54. Kuntz E, Kuntz, Hans-Dieter *Hepatology, Principles and Practice* History, Morphology, Biochemistry, Diagnostics, Clinic, Therapy. Springer. 2006.

55. Park YI, Lee KT, Suh YD, Hyeon T. Upconverting nanoparticles: a versatile platform for wide-field two-photon microscopy and multi-modal in vivo imaging. *Chem Soc Rev.* 2015;44(6):1302-17.

56. Wang L, Lofton C, Popp M, Tan WH. Using luminescent nanoparticles as staining probes for affymetrix GeneChips. *Bioconjugate Chem.* 2007;18(3):610-3.

57. Santra S, Yang H, Dutta D, Stanley JT, Holloway PH, Tan WH, et al. TAT conjugated, FITC doped silica nanoparticles for bioimaging applications. *Chem Commun.* 2004(24):2810-1.

58. Yoo RE, Choi SH, Cho HR, Jeon BS, Kwon E, Kim EG, et al. Magnetic

resonance imaging diagnosis of metastatic lymph nodes in a rabbit model: efficacy of PJY10, a new ultrasmall superparamagnetic iron oxide agent, with monodisperse iron oxide core and multiple-interaction ligands. *PLoS One*. 2014;9(9):e107583.

59. Rangger C, Helbok A, Sosabowski J, Kremser C, Koehler G, Prassl R, et al. Tumor targeting and imaging with dual-peptide conjugated multifunctional liposomal nanoparticles. *International journal of nanomedicine*. 2013;8:4659-71.

60. Xiao W, Luo J, Jain T, Riggs JW, Tseng HP, Henderson PT, et al. Biodistribution and pharmacokinetics of a telodendrimer micellar paclitaxel nanoformulation in a mouse xenograft model of ovarian cancer. *International journal of nanomedicine*. 2012;7:1587-97.

61. Xiao Y, Hong H, Javadi A, Engle JW, Xu W, Yang Y, et al. Multifunctional unimolecular micelles for cancer-targeted drug delivery and positron emission tomography imaging. *Biomaterials*. 2012;33(11):3071-82.

62. Nel AE, Madler L, Velegol D, Xia T, Hoek EMV, Somasundaran P, et al. Understanding biophysicochemical interactions at the nano-bio interface. *Nature Materials*. 2009;8(7):543-57.

63. He X, Nie H, Wang K, Tan W, Wu X, Zhang P. In vivo study of biodistribution and urinary excretion of surface-modified silica nanoparticles. *Anal Chem*. 2008;80(24):9597-603.

64. Thevenot P, Cho J, Wavhal D, Timmons RB, Tang L. Surface chemistry influences cancer killing effect of TiO<sub>2</sub> nanoparticles. *Nanomedicine-Uk*. 2008;4(3):226-36.

65. Johnston HJ, Hutchison GR, Christensen FM, Peters S, Hankin S, Stone V.

Identification of the mechanisms that drive the toxicity of TiO<sub>2</sub> particulates: the contribution of physicochemical characteristics. *Part Fibre Toxicol.* 2009;6.

66. Yong KT, Law WC, Hu R, Ye L, Liu LW, Swihart MT, et al. Nanotoxicity assessment of quantum dots: from cellular to primate studies. *Chem Soc Rev.* 2013;42(3):1236-50.

67. Gao X, Cui Y, Levenson RM, Chung LW, Nie S. In vivo cancer targeting and imaging with semiconductor quantum dots. *Nat Biotechnol.* 2004;22(8):969-76.

68. Lipka J, Semmler-Behnke M, Sperling RA, Wenk A, Takenaka S, Schleh C, et al. Biodistribution of PEG-modified gold nanoparticles following intratracheal instillation and intravenous injection. *Biomaterials.* 2010;31(25):6574-81.

69. Wang YC, Liu YJ, Luehmann H, Xia XH, Brown P, Jarreau C, et al. Evaluating the Pharmacokinetics and In Vivo Cancer Targeting Capability of Au Nanocages by Positron Emission Tomography Imaging. *Acs Nano.* 2012;6(7):5880-8.

70. Liu J, Yu M, Ning X, Zhou C, Yang S, Zheng J. PEGylation and zwitterionization: pros and cons in the renal clearance and tumor targeting of near-IR-emitting gold nanoparticles. *Angew Chem Int Ed Engl.* 2013;52(48):12572-6.

71. Chen J, Glaus C, Laforest R, Zhang Q, Yang M, Gidding M, et al. Gold nanocages as photothermal transducers for cancer treatment. *Small.* 2010;6(7):811-7.

72. Wang Y, Liu Y, Luehmann H, Xia X, Brown P, Jarreau C, et al. Evaluating the pharmacokinetics and in vivo cancer targeting capability of Au nanocages by

- positron emission tomography imaging. *Acs Nano*. 2012;6(7):5880-8.
73. Wang F, Yu L, Monopoli MP, Sandin P, Mahon E, Salvati A, et al. The biomolecular corona is retained during nanoparticle uptake and protects the cells from the damage induced by cationic nanoparticles until degraded in the lysosomes. *Nanomedicine-Uk*. 2013;9(8):1159-68.
74. Chen G, Qiu H, Prasad PN, Chen X. Upconversion nanoparticles: design, nanochemistry, and applications in theranostics. *Chem Rev*. 2014;114(10):5161-214.
75. Gbadamosi JK, Hunter AC, Moghimi SM. PEGylation of microspheres generates a heterogeneous population of particles with differential surface characteristics and biological performance. *FEBS Letters*. 2002;532(3):338-44.
76. Yeung T, Gilbert GE, Shi J, Silvius J, Kapus A, Grinstein S. Membrane phosphatidylserine regulates surface charge and protein localization. *Science*. 2008;319(5860):210-3.
77. Jin JF, Gu YJ, Man CWY, Cheng JP, Xu ZH, Zhang Y, et al. Polymer-Coated NaYF<sub>4</sub>:Yb<sup>3+</sup>, Er<sup>3+</sup> Upconversion Nanoparticles for Charge-Dependent Cellular Imaging. *Acs Nano*. 2011;5(10):7838-47.
78. Jenkins JT, Halaney DL, Sokolov KV, Ma LL, Shipley HJ, Mahajan S, et al. Excretion and toxicity of gold-iron nanoparticles. *Nanomedicine: Nanotechnology, Biology and Medicine*. 2013;9(3):356-65.
79. Lu ZS, Qiao Y, Zheng XT, Chan-Park MB, Li CM. Effect of particle shape on phagocytosis of CdTe quantum dot-cystine composites. *Medchemcomm*. 2010;1(1):84-6.

80. Champion JA, Mitragotri S. Shape Induced Inhibition of Phagocytosis of Polymer Particles. *Pharm Res-Dordr.* 2009;26(1):244-9.
81. Arias IM. Transfer of Bilirubin from Blood to Bile. *Semin Hematol.* 1972;9(1):55.
82. Loberg MD NA, Porter DW. Development of hepatobiliary imaging agents. *Nuclear medicine annual.* 1981:1-33.
83. Varma MV, Obach RS, Rotter C, Miller HR, Chang G, Steyn SJ, et al. Physicochemical space for optimum oral bioavailability: contribution of human intestinal absorption and first-pass elimination. *J Med Chem.* 2010;53(3):1098-108.
84. Takashima T, Wu CY, Takashima-Hirano M, Katayama Y, Wada Y, Suzuki M, et al. Evaluation of Breast Cancer Resistance Protein Function in Hepatobiliary and Renal Excretion Using PET with C-11-SC-62807. *J Nucl Med.* 2013;54(2):267-76.
85. Watanabe T, Fujita M, Awata M, Iida O, Okamoto S, Ishihara T, et al. Integrity of stent polymer layer after drug-eluting stent implantation: in vivo comparison of sirolimus-, paclitaxel-, zotarolimus- and everolimus-eluting stents. *Cardiovasc Interv Ther.* 2014;29(1):4-10.
86. Brust M, Kiely CJ. Some recent advances in nanostructure preparation from gold and silver particles: a short topical review. *Colloids and Surfaces A: Physicochemical and Engineering Aspects.* 2002;202(2-3):175-86.
87. Wolfgang G. Kreyling AMA, Zulqurnain Ali, Alexander Wenk,, Frauke Alves MG, Stephanie Hirn, Raimo Hartmann, Karsten Kantner,, Nadine Haberl DJdA, Gülnaz Khadem-Saba, Jose-Maria, Montenegro JR, Teofilo Rojo, Idoia

Ruiz de Larramendi, Roser Ufartes,, Parak WJ. In vivo integrity of polymer-coated gold nanoparticles. *Nature Nanotech.* 2015.

88. Peng J, Sun Y, Zhao L, Wu Y, Feng W, Gao Y, et al. Polyphosphoric acid capping radioactive/upconverting NaLuF<sub>4</sub>:Yb,Tm,153Sm nanoparticles for blood pool imaging in vivo. *Biomaterials.* 2013;34(37):9535-44.

89. Wang J, Byrne JD, Napier ME, DeSimone JM. More Effective Nanomedicines through Particle Design. *Small.* 2011;7(14):1919-31.

90. Kou L, Sun J, Zhai Y, He Z. The endocytosis and intracellular fate of nanomedicines: Implication for rational design. *Asian Journal of Pharmaceutical Sciences.* 2013;8(1):1-10.

91. Rappoport JZ. Focusing on clathrin-mediated endocytosis. *Biochem J.* 2008;412:415-23.

92. Benmerah A, Lamaze C. Clathrin-coated pits: vive la difference? *Traffic.* 2007;8(8):970-82.

93. Rejman J, Oberle V, Zuhorn IS, Hoekstra D. Size-dependent internalization of particles via the pathways of clathrin- and caveolae-mediated endocytosis. *Biochem J.* 2004;377(Pt 1):159-69.

94. Parton RG, Simons K. The multiple faces of caveolae. *Nat Rev Mol Cell Bio.* 2007;8(3):185-94.

95. Guo CJ, Wu YY, Yang LS, Yang XB, He J, Mi S, et al. Infectious Spleen and Kidney Necrosis Virus (a Fish Iridovirus) Enters Mandarin Fish Fry Cells via Caveola-Dependent Endocytosis. *J Virol.* 2012;86(5):2621-31.

96. Verma A, Stellacci F. Effect of Surface Properties on Nanoparticle-Cell

Interactions. *Small*. 2010;6(1):12-21.

97. Conner SD, Schmid SL. Regulated portals of entry into the cell. *Nature*. 2003;422(6927):37-44.

98. Chithrani BD, Chan WC. Elucidating the mechanism of cellular uptake and removal of protein-coated gold nanoparticles of different sizes and shapes. *Nano Lett*. 2007;7(6):1542-50.

99. Panyam J, Labhasetwar V. Dynamics of endocytosis and exocytosis of poly(D,L-lactide-co-glycolide) nanoparticles in vascular smooth muscle cells. *Pharm Res*. 2003;20(2):212-20.

100. Panyam J, Zhou WZ, Prabha S, Sahoo SK, Labhasetwar V. Rapid endo-lysosomal escape of poly(DL-lactide-co-glycolide) nanoparticles: implications for drug and gene delivery. *Faseb J*. 2002;16(10):1217-26.

101. Buckmaster MJ, Lo Braico D, Jr., Ferris AL, Storrie B. Retention of pinocytized solute by CHO cell lysosomes correlates with molecular weight. *Cell Biol Int Rep*. 1987;11(7):501-7.

102. Jiang X, Rocker C, Hafner M, Brandholt S, Dorlich RM, Nienhaus GU. Endo- and exocytosis of zwitterionic quantum dot nanoparticles by live HeLa cells. *Acs Nano*. 2010;4(11):6787-97.

103. Fang CY, Vijayanthimala V, Cheng CA, Yeh SH, Chang CF, Li CL, et al. The exocytosis of fluorescent nanodiamond and its use as a long-term cell tracker. *Small*. 2011;7(23):3363-70.

104. Jin H, Heller DA, Sharma R, Strano MS. Size-Dependent Cellular Uptake and Expulsion of Single-Walled Carbon Nanotubes: Single Particle Tracking and a

- Generic Uptake Model for Nanoparticles. *Acs Nano*. 2009;3(1):149-58.
105. Chithrani BD, Ghazani AA, Chan WCW. Determining the size and shape dependence of gold nanoparticle uptake into mammalian cells. *Nano Letters*. 2006;6(4):662-8.
106. Zhang SL, Li J, Lykotrafitis G, Bao G, Suresh S. Size-Dependent Endocytosis of Nanoparticles. *Adv Mater*. 2009;21(4):419.
107. Cebrian V, Martin-Saavedra F, Yague C, Arruebo M, Santamaria J, Vilaboa N. Size-dependent transfection efficiency of PEI-coated gold nanoparticles. *Acta Biomater*. 2011;7(10):3645-55.
108. Jiang W, Kim BYS, Rutka JT, Chan WCW. Nanoparticle-mediated cellular response is size-dependent. *Nat Nanotechnol*. 2008;3(3):145-50.
109. Yuan HY, Li J, Bao G, Zhang SL. Variable Nanoparticle-Cell Adhesion Strength Regulates Cellular Uptake. *Phys Rev Lett*. 2010;105(13).
110. Chithrani BD, Chan WCW. Elucidating the mechanism of cellular uptake and removal of protein-coated gold nanoparticles of different sizes and shapes. *Nano Letters*. 2007;7(6):1542-50.
111. Canton I, Battaglia G. Endocytosis at the nanoscale. *Chem Soc Rev*. 2012;41(7):2718-39.
112. Champion JA, Mitragotri S. Role of target geometry in phagocytosis. *P Natl Acad Sci USA*. 2006;103(13):4930-4.
113. Sakhtianchi R, Minchin RF, Lee K-B, Alkilany AM, Serpooshan V, Mahmoudi M. Exocytosis of nanoparticles from cells: Role in cellular retention and toxicity. *Advances in Colloid and Interface Science*. 2013;201–202(0):18-29.

114. Yanes RE, Tarn D, Hwang AA, Ferris DP, Sherman SP, Thomas CR, et al. Involvement of Lysosomal Exocytosis in the Excretion of Mesoporous Silica Nanoparticles and Enhancement of the Drug Delivery Effect by Exocytosis Inhibition. *Small*. 2013;9(5):697-704.
115. Ferrati S, Mack A, Chiappini C, Liu X, Bean AJ, Ferrari M, et al. Intracellular trafficking of silicon particles and logic-embedded vectors. *Nanoscale*. 2010;2(8):1512-20.
116. Wang Z, Li N, Zhao J, White JC, Qu P, Xing B. CuO nanoparticle interaction with human epithelial cells: cellular uptake, location, export, and genotoxicity. *Chem Res Toxicol*. 2012;25(7):1512-21.
117. Chu Z, Huang Y, Tao Q, Li Q. Cellular uptake, evolution, and excretion of silica nanoparticles in human cells. *Nanoscale*. 2011;3(8):3291-9.
118. Stayton I, Winiarz J, Shannon K, Ma YF. Study of uptake and loss of silica nanoparticles in living human lung epithelial cells at single cell level. *Analytical and Bioanalytical Chemistry*. 2009;394(6):1595-608.
119. Harush-Frenkel O, Rozentur E, Benita S, Altschuler Y. Surface Charge of Nanoparticles Determines Their Endocytic and Transcytotic Pathway in Polarized MDCK Cells. *Biomacromolecules*. 2008;9(2):435-43.
120. Asati A, Santra S, Kaittanis C, Perez JM. Surface-Charge-Dependent Cell Localization and Cytotoxicity of Cerium Oxide Nanoparticles. *ACS Nano*. 2010;4(9):5321-31.
121. Cho EC, Xie J, Wurm PA, Xia Y. Understanding the Role of Surface Charges in Cellular Adsorption versus Internalization by Selectively Removing

Gold Nanoparticles on the Cell Surface with a I2/KI Etchant. *Nano Letters*. 2009;9(3):1080-4.

122. Wang C, Tao H, Cheng L, Liu Z. Near-infrared light induced in vivo photodynamic therapy of cancer based on upconversion nanoparticles. *Biomaterials*. 2011;32(26):6145-54.

123. Lee DS, Im HJ, Lee YS. Radionanomedicine: widened perspectives of molecular theragnosis. *Nanomedicine-Uk*. 2015.

## 국 문 초 록

# 마이셀 피막화된 Upconverting 나노입자의 체내 PET과 광학영상을 이용한 향상된 간담체 배설

서효정

서울대학교

융합과학기술대학원 분자의학 및 바이오제약학과

### 목적

나노입자를 생의학분야에 응용하려는 많은 시도가 있었으나, 나노입자는 생체내 여러 장기에 침착 되어 독성을 일으킨다. 따라서, 나노입자를 생의학분야에 사용하기 위해서는 생체적합성이 좋으며, 체외로 배출이 빨리 되는 것이 중요하다. 최근 생의학분야의 후보

물질로 upconverting 나노입자가 대두되었다. 본 연구에서는 양전자단층촬영 (PET) 과 unconversion 광학영상 (ULI)을 통하여 마이셀 피막화된  $^{64}\text{Cu}$  를 표지 한 unconverting 나노입자 ( $^{64}\text{Cu}$ -NOTA-UCNPs)가 24 시간 내에 빠른 간담체 배설을 보이는 것을 관찰하였다.  $^{64}\text{Cu}$  는 반감기가 762 분으로 길어서, 72 시간 동안 생체내 분포를 관찰할 수 있는 방사성동위원소이다. 또한, PET 과 감마카운터를 이용하여 각 장기별로 값을 정량할 수 있다. 따라서, PET 과 체외 기법을 이용하여 마이셀 피막화된  $^{64}\text{Cu}$ -NOTA-UCNPs 의 배설을 정량적으로 평가하였다. PET, ULI, 투과전자현미경 (TEM) 을 이용하여 마이셀 피막화된  $^{64}\text{Cu}$ -NOTA-UCNPs 배설경로를 밝혔다.

## 방법

$\text{NaYF}_4:\text{Yb}^{3+}, \text{Er}^{3+}$  nanoparticles (UCNPs) 은 NOTA- $\text{C}_{18}$  과  $^{64}\text{Cu}$  로 피막화 하였다. 마이셀 피막화된  $^{64}\text{Cu}$ -NOTA-UCNPs 를 6 주령의 수컷 BALB/c 누드마우스 (무게 =  $24.1 \pm 0.5$  g, 용량 =  $40 \pm 0.6$   $\mu\text{Ci}/50$   $\mu\text{L}$ , 수 = 7) 의 꼬리혈관 내에 주사한 후, 전신 마이크로 PET 을 촬영하였다. 연속적인 시간 별 체내영상을 획득하여(0.25, 1, 2, 4, 8, 와 24 시간, 수 = 3 / 0.25, 1, 2, 4, 8, 24, 48 과 72 시간, 수 = 4) 체내분포를 분석하였다. 리간드가 떨어지는지 여부를 확인하기 위해, 유리  $^{64}\text{Cu}$  (수 = 3),  $^{64}\text{Cu}$ -NOTA- $\text{C}_{18}$  (수 = 3),  $^{64}\text{Cu}$ -NOTA-UCNPs

(수 = 7) 를 주입한 누드마우스의 마이크로 PET 비교 연구를 시행하였다. 연속적인 시간 별 체내 영상을 (0.25, 1, 2, 4, 8, 과 24 시간) 마이크로 PET 을 이용하여 획득하였다. 체외분포 분석을 위해 BALB/c 누드마우스 (무게 =  $20.1 \pm 0.5$  g, 용량 =  $1 \mu\text{Ci}/100 \mu\text{L}$ ) 의 꼬리혈관에 마이셀 피막화된  $^{64}\text{Cu-NOTA-UCNPs}$  를 주사하였다. 주사 후 BALB/c 누드마우스를 각각 시간대별로 희생하여 장기를 적출하였다 (1, 4, 8, 24 과 72 시간, 대변 및 소변 수집을 위해 3 마리, 각 시간대별 수 = 3, 전체 수 = 18). ULI 생체분포 연구를 위해, 마이셀 피막화된  $^{64}\text{Cu-NOTA-UCNPs}$  를 BALB/c 누드마우스 (무게 =  $24.1 \pm 0.5$  g, 용량 =  $0.158 \text{ mg}/300 \mu\text{L}$ , 전체수 = 7) 에 주사하였다. 각각 시간대별로 체내, 정위치, 체외 ULI 를 획득하였다 (1, 2, 4, 8 과 24 시간). 마이크로 PET 과 ULI 를 이용하여 24 시간동안 모은 대변과 소변의 마이셀 피막화된  $^{64}\text{Cu-NOTA-UCNPs}$  의 배출을 평가하였다. TEM 을 이용하여 2 개의 시간대에서 (1 시간, 수 = 3, 24 시간, 수 = 4) 적출한 간을 살펴보았으며 간담체 배설을 관찰하였다.

## 결과

마이셀 피막화된  $^{64}\text{Cu-NOTA-UCNPs}$  기법의 최종수율은 40% 였다. 마이셀 피막화된  $^{64}\text{Cu-NOTA-UCNPs}$  의 방사화학 순도는 99% 였다. 마이셀 피막화된  $^{64}\text{Cu-NOTA-UCNPs}$  의 간담체 배설은

24 시간내에 빨리 진행되었다. 마이크로 PET 상에서 간의 섭취는 8 시간까지 지속되었으나, 24 시간에서는 현저한 감소를 보였고, 72 시간에서는 섭취가 더욱 감소하였다. 1 시간후에는 장관을 따라 선형의 증가된 섭취가 관찰되었으며, 2 시간, 4 시간, 8 시간 지연영상에서는 더욱 확장된 장관의 섭취가 관찰되었다. 또한, 마이셀 피막화된  $^{64}\text{Cu}$ -NOTA-UCNPs 는 유리  $^{64}\text{Cu}$  보다 빠른 간의 배설을 보였으며,  $^{64}\text{Cu}$ -NOTA- $\text{C}_{18}$ 와는 달리 소변으로의 배설이 극히 적었다.

마찬가지로, 체외 분포 실험에서 초기 간 섭취의 80%가 72 시간내에 제거되었다. 또한, 주사 후 24 시간내에 대변 배설을 통해서 마이셀 피막화된  $^{64}\text{Cu}$ -NOTA-UCNPs 의 40.9%가 제거되었다. 간의 섭취는 8 시간까지 증가하다가, 24 시간에서 현저히 감소하였다. 장관은 8 시간까지 단계적으로 증가되는 섭취를 보였으며, 24 시간에서 감소하였다.

또한, ULI 영상은 체내, 정위, 체외 실험에서 빠른 간담체 배설을 나타내었다. 그러나, 체내 ULI 영상은 PET영상과 ( $12 \mu\text{g}/\text{생쥐}$ ) 보다 13배나 높은 양 ( $158 \mu\text{g}/\text{생쥐}$ ) 을 주입해야 영상에 적합한 신호를 획득할 수 있었다. 주사후 1시간 영상에서, 체외 영상은 간, 비장, 폐의 양성 신호를 보였으며, 이것은 PET 영상과 같은 결과였다. 체내영상에서는 장관의 섭취는 잘 보이지 않았으나, 장관을 적출하여 슬라이드 글라스에 펼친 후에는 빛 투과율이 높아져, 장관으로 배설되는

UCNP의 높은 신호를 관찰 할 수 있었다.

추가적으로, 마이셀 피막화된  $^{64}\text{Cu-NOTA-UCNPs}$ 의 간담체배설의 증거를 대변과 소변을 통하여 관찰하였다. ULI에서 모은 대변과 소변에서 UCNP의 신호를 관찰하였다. PET 영상은 배출된 대변에서 마이셀 피막화된  $^{64}\text{Cu-NOTA-UCNPs}$ 에 의한 높은 섭취를 보여주었다. 주사 후 1시간 TEM 영상에서, UCNPs는 간의 동모양혈관내, 디체강, 간세포, 쿠퍼세포, 담즙세관에서 다수 관찰되었다. 그러나, 주사 후 24시간 TEM 영상에서는 간세포내에 UCNPs가 관찰되지 않았으며, 일부 쿠퍼세포에서만 관찰되었다.

## 결론

결론적으로, 본 연구는 마이크로 PET, ULI 및 체외 기법을 통하여 마이셀 피막화된  $^{64}\text{Cu-NOTA-UCNPs}$  이 빠른 간담체 배설을 보임을 밝혔다. PET과 ULI의 이중영상은 나노입자의 배설을 관찰하는데 이상적이다. 특히 PET은 체내분포를 정확히 정량할 수 있고, ULI는 UCNP를 확인하는데 사용할 수 있다. 더욱이, 본 연구는 마이셀 피막화된  $^{64}\text{Cu-NOTA-UCNPs}$ 가 ULI와 PET으로 이중영상으로 구현됨을 보였으며, 간담체 배출이 빠른 것을 규명하였다. 이러한 특성은 기능적인 성질을 추가하여 향후 다양한 분야에 응용이 가능하다.

**주요어:** Upconverting 나노입자, 양전자단층촬영 (PET), 광학영상, 간담체 배설, 투과전자현미경 (TEM)

**학번:** 2012-30798